SMOG2 Technical Proposal

V. Carassiti[1], G. Ciullo[1,2], P. Di Nezza[3], P. Lenisa[1,2],
L. L. Pappalardo[1,2], E. Steffens[4], A. Vasilyev[5]
C. Boscolo Meneguolo[6], G. Bregliozzi[6], R. Bruce[6], P.M. Gebolis[6], G. Iadarola[6],
L. Mether[6], G. Pigny[6], B.K. Popovic[6], B. Salvant[6], J. Sestak[6], C. Vollinger[6], C. Zannini[6]

[1] *Istituto Nazionale di Fisica Nucleare, Sezione di Ferrara, 44122 Ferrara, Italy*
[2] *Dipartimento di Fisica e Scienze della Terra, Università di Ferrara, 44122 Ferrara, Italy*
[3] *Istituto Nazionale di Fisica Nucleare, Laboratori Nazionali di Frascati, 00044 Frascati, Italy*
[4] *Physikalisches Institut, Universität Erlangen-Nürnberg, 91058 Erlangen, Germany*
[5] *Petersburg Nuclear Physics Institute, Gatchina, Leningrad Oblast,188300, Russia*
[6] *European Organization for Nuclear Research (CERN), Geneva, Switzerland*

Abstract

A proposal for an upgraded version of the existing gas injection system for the LHCb experiment (SMOG) is presented. The core idea of the project, called SMOG2, is the use of a storage cell for the injected gas to be installed upstream of the VELO detector. The main advantage of the proposed system is to increase by up to two orders of magnitude the effective target areal density, thus resulting in a significant increase of the luminosity for fixed-target collisions. Other important advantages are the possibility to inject additional gas species, including H_2 and D_2, a better defined interaction region, displaced with respect to the nominal interaction point, and thus possibly compatible with running in parallel to the collider mode (resulting in a substantial increase in integrated luminosity). A technical design of the target system is presented together with a description of the installation procedure. Impedance and dynamic vacuum effects have been studied and will be mitigated by the use of suitable wake field suppressors and low secondary electron yield coatings. The geometry of the system has been integrated into the GEANT4 model of the LHCb detector in order to validate the target design with reliable simulation studies, and to ensure that the near-beam material budget has negligible effects in terms of beam-induced background. The loss in reconstruction efficiency with respect to SMOG for selected physics channels, due to the displaced interaction region with respect to the nominal interaction point, is found to be of the order 10%, thus largely compensated by the expected increase in luminosity. It is proposed to install the new system during LHC Long Shutdown 2. This will open new physics frontiers at LHCb already from the LHC Run-3.

Contents

1   Introduction

LHCb is the only LHC detector that can run both in collider and fixed-target mode. The LHCb fixed-target system, called SMOG (System for Measuring the Overlap with Gas) [1], was originally conceived for precise colliding-beams luminosity calibration. The SMOG system allows to inject a low flow rate of noble gas into the vacuum vessel of the LHCb VErtex LOcator (VELO) detector [2]. A temporary local pressure bump of about 10^{-7} mbar is obtained in the LHCb beam-pipe section (over a length of about 40 m around the interaction point), which is about two orders of magnitude higher than the nominal LHC vacuum pressure and one order of magnitude lower than the LHC vacuum interlocks limit. The resulting beam-gas collision rate (also increased by two orders of magnitude) allows for a precise determination of the beam density profiles. This has been successfully exploited to obtain very precise luminosity measurements through the beam-gas imaging technique [1, 3, 4].

As an additional important feature, SMOG gives the unique opportunity to operate an LHC experiment in a fixed target mode, and to study proton-nucleus and nucleus-nucleus collisions on various target types and at different center-of-mass energies. Several dedicated runs have already been performed since 2015 using He, Ar, or Ne targets with proton and lead beams at energies ranging from 2.5 TeV to 6.5 TeV, as shown in Fig. 1. This allowed to disclose a new, rich and ambitious physics program at the LHC, exploiting the unique fixed-target kinematics achievable with beam energies at the TeV scale. Physics searches with SMOG include study of cold nuclear-matter effects through prompt heavy-flavour production in pA collisions [5], Quark Gluon Plasma (QGP) formation in PbA collisions, search for intrinsic charm in the proton at high Bjorken-x, as well as measurements of prompt antiproton production in pHe collisions [6], of relevance for Dark Matter searches in astrophysics.
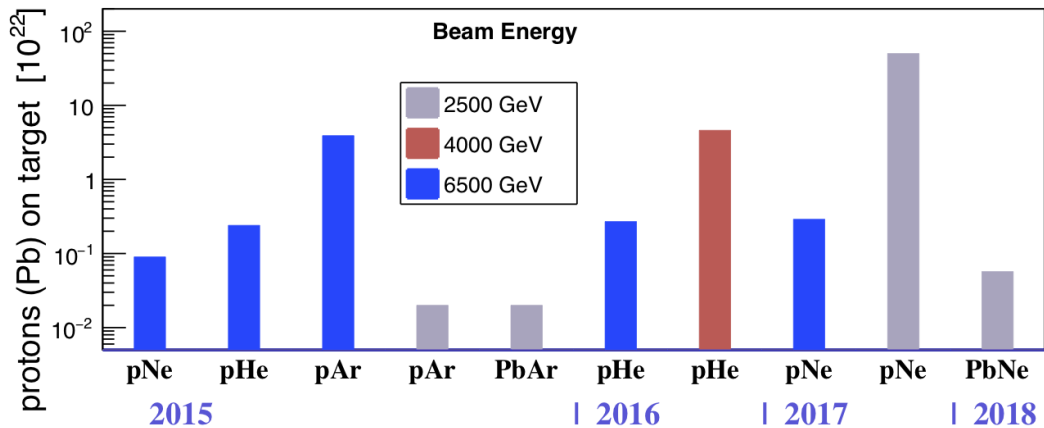
Figure 1:   Dedicated SMOG runs collected since 2015. Beam-gas collisions have been recorded using different gas types (He, Ar, Ne) and beam energies.

The SMOG2 project, presented in this document, constitutes an upgrade of the actual SMOG system. The core idea of SMOG2 is the use of a storage cell for the injected gas, to be installed at the upstream edge of the VELO, coaxial with the LHC beam. The proposed plan is to install the SMOG2 setup during the LHC Long Shutdown 2 (LS2).

The main advantage of SMOG2 is the possibility to reach effective areal densities (and thus luminosities) higher by a factor of about 8 (H_2) to 35 (Ar) with respect to SMOG by injecting the same flow rate (see Tab. 1). A further increase of densities could be considered if compatible with the spectrometer occupancy. Other important advantages compared to SMOG are:

- a more sophisticated Gas Feed System (GFS), which will allow for a significantly more precise determination of the target density (and luminosity);

- the possibility to inject other noble gas species as well as H_2 and D_2. In particular, the use of H_2 and D_2 targets, available for the first time at the LHC, will open new physics frontiers that includes the study of the proton structure in terms of quark and gluons distributions at unique kinematic conditions;

- a significantly better defined interaction region (determined by the cell length of 20 cm);

- the possibility to exploit all circulating beam bunches for fixed-target physics (i.e. to run in parallel to the collider mode) if the beam–gas interactions are proved to generate a tolerable background to the mainstream pp physics, thanks to the displaced interaction region with respect to the nominal collider IP.

A detailed physics program with a fixed target at LHCb is presented in a dedicated report of the Physics Beyond Collinders study group, Ref. [7]. The SMOG2 project presents different challenges, that are addressed in this document. In particular, the storage cell has to fulfil various requirements:

- it must fit into the limited space available inside the existing VELO vessel, upstream of the VELO detector;

- it must be openable (consisting of two halves), such to rigidly follow the motion of the two halves of the VELO detector (open position during beam injection and tuning, closed position during normal lumi operation);

- it must be light and thin, in order to keep the impact of the material budget in the proximity of the beam at a negligible level;

- it must ensure sufficient gas tightness along the sides in closed position, when the gas is flowing;

- it must have an openable system of Wake Field Suppressors (WFS) to ensure electrical continuity along the beam pipe and suppression of the wake fields;

- it must be properly coated to avoid instabilities by the formation of Electron Clouds.

Furthermore, special care has to be devoted to the study of the beam-cell interaction and the impact of the Machine Induced Background (MIB) on the target material. Finally, since the interaction region will be displaced in average 40 cm upstream from the nominal interaction region ($z = 0$), and essentially limited to the cell length, different acceptance and reconstruction efficiencies are expected with respect to SMOG. A comparative study for the case of two relevant physics channels, reported in Sect. 9, demonstrates that the decrease in reconstruction

efficiency for SMOG2 is relatively small (of the order of 10%) and thus largely compensated by the significantly higher target areal density and, possibly, by exploiting all circulating bunches.

The scope of this document is to focus on a detailed description of the SMOG2 project and technical design, while sketching out the physics potential. The actual usage of SMOG2 in terms of run time and gas species is left for future discussions that will involve physics arguments as well as impact management for the LHCb core physics program and for the LHC machine operation.

This document is organized as follows: in Sect. 2 a brief description of the SMOG system and of the VELO detector is presented. Section 3 is dedicated to the description of the proposed upgraded system (SMOG2). Issues related to the interaction with the machine are discussed in Sect. 4. The description of the mechanical design and the construction of prototypes is addressed in Sect. 5, followed by the description of the new proposed gas feed system, reported in Sect. 6. The installation procedure is described in Sect. 7. The implementation of the storage cell geometry in GEANT4 and simulation studies of Machine Induced Background are presented in Sect. 8. Section 9 reports simulation studies on reconstruction efficiencies for selected physics channels, followed by the projected performances of SMOG2, presented in Sect. 10. The time schedule of the project and the responsibilities are presented in Sect. 11. Finally, summary and conclusions are presented in Sect. 12.

2   The SMOG System and the VELO Detector

The SMOG gas injection system, shown in Fig. 2, was developed and commissioned in the LHCb experiment with the purpose of significantly increasing the beam-gas collision rate (Fig. 3) in order to take full advantage of the beam-gas imaging capabilities for precision luminosity measurements [1, 3, 4]. During operation, a low noble–gas flow rate is injected into the LHC beam pipe, inside the VELO vessel (Fig. 4), raising the LHC vacuum pressure by two orders of magnitude (from about 10^{-9} mbar to slightly above 10^{-7} mbar). During the gas injection, the two VELO vacuum ion pumps located right under the interaction point are switched off and the VELO beam vacuum is opened to an annex volume pumped by a turbomolecular pump previously stabilized at the nominal gas pressure. When gas injection is stopped and the ion pumps are switched back on, the nominal pressure of 10^{-9} mbar is recovered in a matter of minutes.

A sketch of the SMOG system is shown in Fig. 5. A turbo pump (TP 301) is connected via the gate valve GV302 to the VELO vessel. By keeping the valve closed, a gas with flow rate Q is injected into the pump, resulting in a pressure $p_0 = Q/S$, where S is the pumping speed of the TP301, of about 500 l/s. When opening the valve, the VELO beam vacuum pressure evolves to the same value p_0. During SMOG operation, all other pumps acting on the VELO beam vacuum vessel are switched off. The injected gas pressure can be monitored by four cold-cathode gauges (Penning type) and one hot filament ionization gauge (Bayard-Alpert type) located at various positions around the VELO. The absolute calibration of the Penning gauges exhibits a variability at ± 50 % level, so that a precise direct measurement of the target gas density is presently not possible. The Bayard-Alpert gauge was calibrated and may give a density measurement at the $\pm 10\%$ level.

The VELO detector [2] has played an essential role in all measurements with SMOG. The
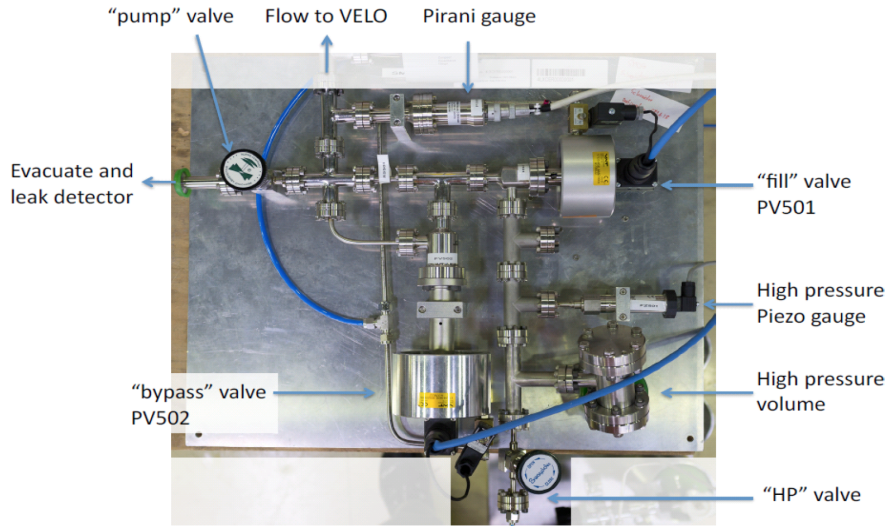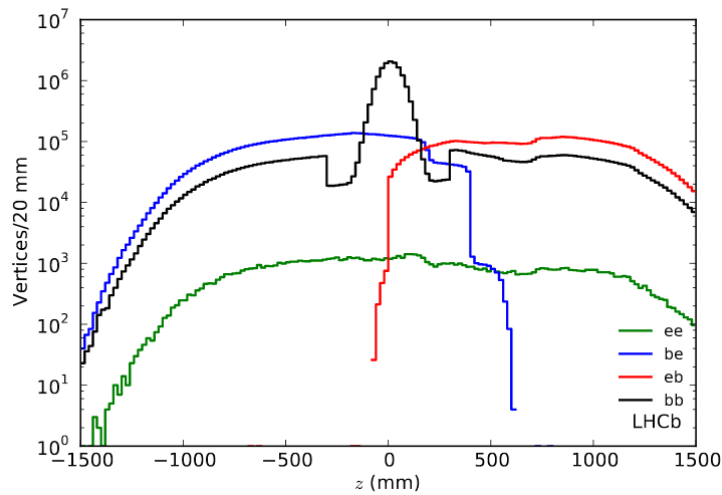
Figure 2: The SMOG gas feed system.

Figure 3: Example of longitudinal distribution of vertices for the various bunch crossing types. Crossing types ee (green), be (blue) and eb (red) contain only beam-gas events while the bb crossing type (black) contains beam-beam vertices in the central region and beam-gas vertices over the whole range [1].

upgraded VELO detector [8, 9], designed to cope with the expected increased luminosity, will be installed during the LHC LS2. The VELO sensors are placed at a radial distance from the beam which is smaller than the aperture required by the LHC during injection, and must therefore be retractable. For this reason the VELO is split in two halves, which are moved inward or outward with respect to the beam axis, allowing for safe beam injection and tuning operations. The two detector halves are installed inside the VELO vessel (Fig. 4), which has the purpose of keeping
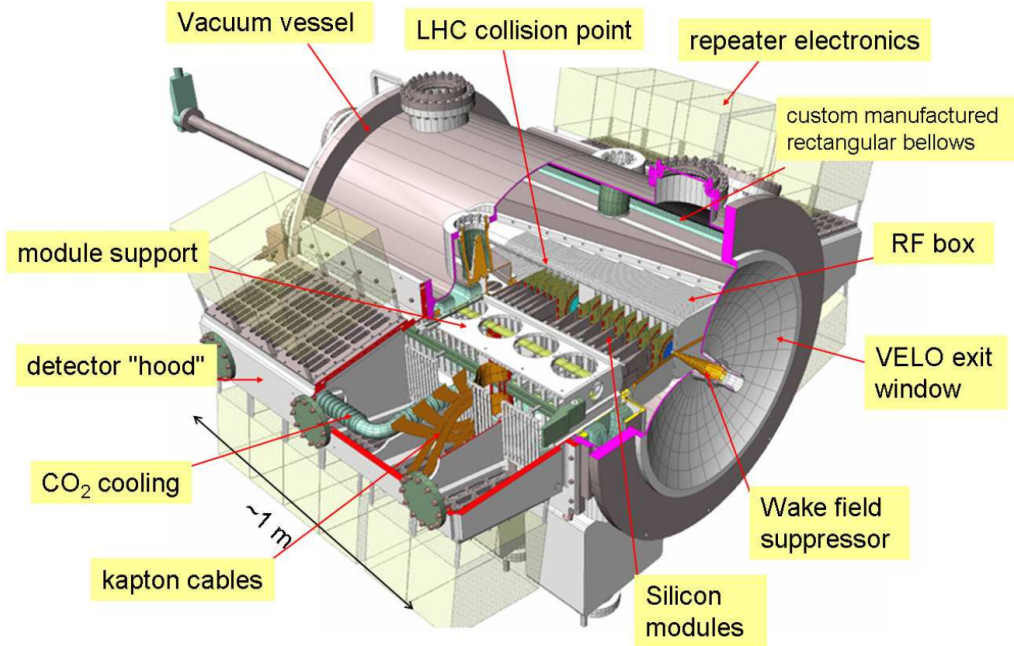
Figure 4: Sketch of the VELO vessel fully equipped with the VELO silicon modules, RF box, electronics and supporting services.

the sensors in vacuum, and is separated from the machine vacuum by a thin walled corrugated aluminum sheet (RF foil).

3 Principle of the SMOG2 Gas Target

This section describes the working principle of the SMOG2 setup, designed for 2nd generation fixed-target measurements with the LHCb detector.

3.1 The storage cell concept

The use of a tubular storage cell coaxial with the beam is the optimal choice for a gas target since, given a certain gas input, it allows to maximize the areal density θ seen by the beam. The principle is shown in Fig. 6. The open-ended cylindrical tube has an inner diameter D and a length L. Gas at flow rate Q, provided by a GFS (described in Sect. 6), is injected via capillary at the center of the storage cell.

The volume density ρ_0 at the center is given by

$$\rho_0 = \frac{\Phi}{C_{tot}}, \tag{1}$$

where Φ is the particle flux (particles/s) of the gas flow and C_{tot} the total conductance of the tube from the center outwards. In this specific case, C_{tot} is given by the conductance of two
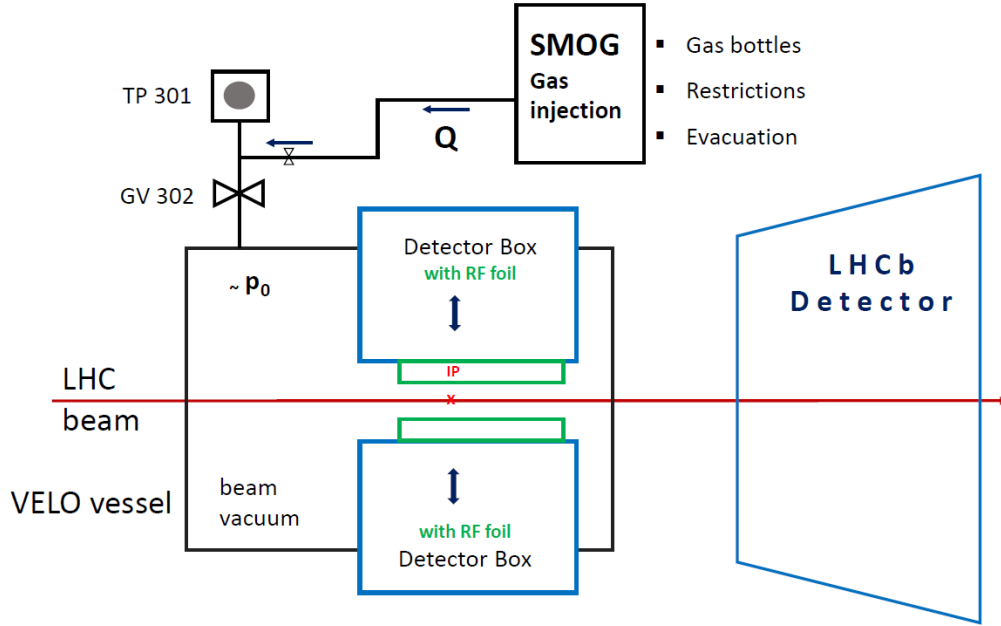
Figure 5: Principle of the SMOG system, consisting of a gas feed system (Fig. 2) injecting into a pump (TP 301). With valve GV 302 open, the VELO vessel is filled with gas at low density, determined by the injected flow rate.
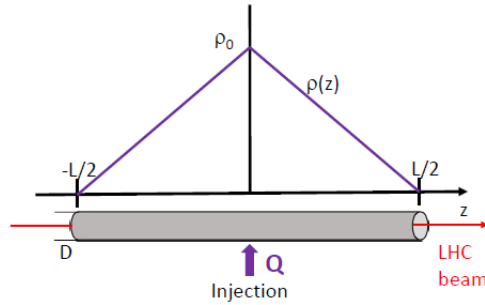
Figure 6: Scheme of a tubular storage cell of length L and inner diameter D. Injection is in the center with flow rate Q, resulting in a triangular density distribution $\rho(z)$ with maximum ρ_0 at the center.

consecutive tubes of length $L/2$. For cylindrical tubes, the conductance in the molecular flow regime is given by [11]:

$$C(\text{l/s}) = 3.81 \sqrt{T/M} \ \frac{D^3}{L + 1.33 \, D} \ , \tag{2}$$

where L, D are expressed in cm, the temperature T in K, and M is the molecular mass number. The areal density is given by:

$$\theta = \frac{1}{2}\rho_0 L. \tag{3}$$

A tube-like storage cell to be installed within the VELO vessel has to meet the following minimal requirements:

1. Has to be split in two halves, movable apart during beam injection, energy ramp, squeeze and adjustments of the beam. The two halves must be connected with the respective VELO boxes and moved simultaneously.

2. Must have conducting surfaces surrounding the beam, needed to shield the chamber from the beam RF fields, thus preventing excitation of wake fields. In this specific case these are provided by the cell structure itself, a conducting transition to the RF foil, and a flexible connection to the beam tube suspended by the elliptical flange of the VELO vessel.

3. Must be connected to a gas injection system feeding directly into the storage cell center via a flexible line.

4. Must include temperature measurement for each cell half. Because of the $\sqrt{T}$ dependence of the conductance (Eq. (2)), T has to be measured precisely in order to determine the target areal density θ through Eqs. (1) and (3).

Furthermore, additional pumping on the VELO vessel may be applied, in contrast to SMOG, without affecting the target density. This will have a beneficial effect on the background conditions.

The scheme of the SMOG2 gas target with its storage cell and GFS is shown in Fig. 7.

3.2 Gas flow and expected performance

For the present design of the SMOG2 target cell, the following parameters are assumed:

1. open-ended tubular cell with inner diameter $D = 1.0$ cm;

2. full length $L = 20$ cm;

3. temperature $T \simeq 300$ K.

Using Eq. (2) one obtains a total conductance $C_{tot} = 5.82$ l/s for He ($M = 4$). The particle flux corresponding to the He gas flow of Ref. [6] is[1] $\Phi = 3.5 \cdot 10^{15}$ particles/s. From Eq. (1) one then obtains a target areal density of $6.0 \cdot 10^{12}$ atoms/cm^2, which is more than 10 times higher than the SMOG He areal density of $5.6 \cdot 10^{11}$ atoms/cm^2 extracted from the information provided in Ref. [6].

In Table 1, SMOG2 target parameters are shown for various gas species, by assuming reasonable target areal densities. In addition, SMOG densities for the same flow rates are shown, together with the SMOG2/SMOG density ratios, illustrating the improvement achievable using a storage cell. The variation of this ratio with M_{gas} (molecular weight) comes from the $M^{-1/2}$ dependance of C_{tot} (Eq. (2)), therefore the improvement is highest for the heavy gases.

---

[1]This value has been extracted from the He density of $Q_{He} = 1.3 \cdot 10^{-4}$ mbar l/s, corresponding to the pressure of $2.6 \cdot 10^{-7}$ mbar reported in Ref. [6], assuming a pumping speed on the VELO vessel of S $= 500$ l/s, a fiducial interaction region of 0.8 m in length and a temperature of 300 K.
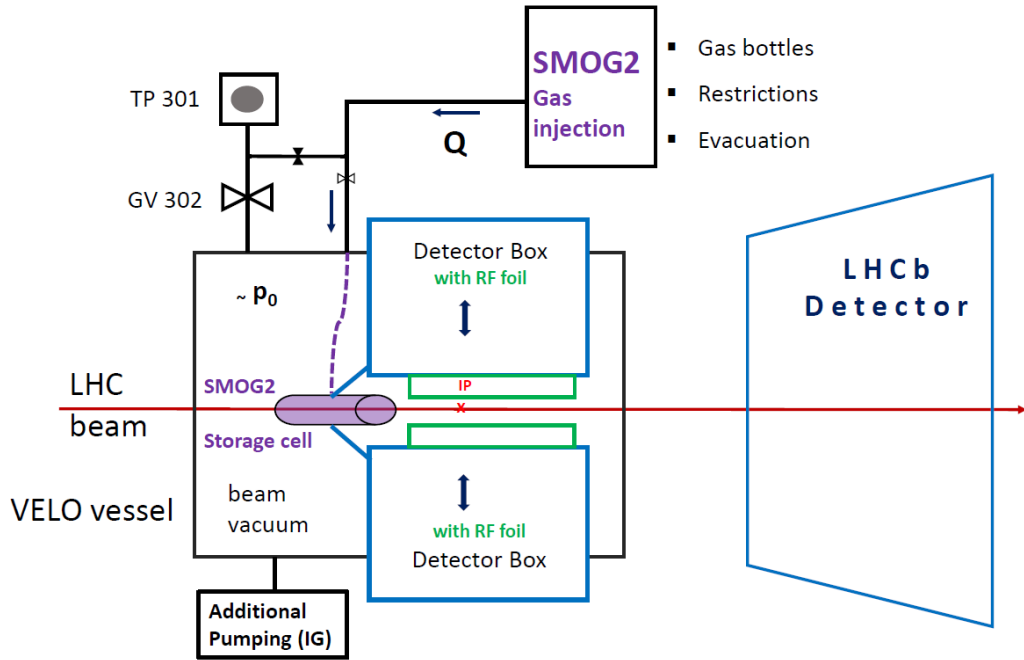
Figure 7: Sketch of the SMOG2 system. The gas is injected via capillary at the center of the storage cell.

Table 1: Typical SMOG2 areal densities for different gas species and the resulting target parameters (intensity and flow rate). For comparison, the corresponding SMOG densities are also reported, assuming the same flow rate, a pumping speed on the VELO vessel of 500 l/s and a fiducial region of 0.8 m (as in Ref.[6]).

Gas species	He	Ne	Ar	Kr	Xe	H_2	D_2	N_2	O_2
SMOG2 areal density (10^{12} atoms/cm^2)	10	10	10	5	5	10	10	10	10
Intensity (10^{15} particles/s)	5.80	2.58	1.82	1.36	1.01	4.08	2.89	1.09	1.03
Flow rate (10^{-5} mbar · l/s)	21.4	9.6	6.8	4.68	3.75	15.02	10.07	4.05	3.83
SMOG areal density (10^{12} atoms/cm^2)	0.92	0.41	0.29	0.20	0.16	1.30	0.92	0.35	0.33
SMOG2/SMOG	10.9	24.4	34.5	25.0	31.3	7.7	10.9	28.6	30.3

In addition, with the pumps on the VELO vessel switched on, one might be able to run at a considerably higher flow injected into the storage cell, thus increasing the target density even further. This has to be studied in detail, taking into account pumping speed and capacity of the vacuum system of the VELO vessel for the different gases (noble/inert, active).

4 Machine Issues

The installation of an openable narrow Aluminum tube of 5 mm inner radius inside the VELO vessel near the detector boxes requires to check carefully for potential risks related to:

- aperture required for the beam;

- impedance of the system of WFS's and possible heating and beam instabilities;

- electron cloud and ion build-up phenomena;

An additional important aspect to be considered is the impact of the SMOG2 gas target on the beam lifetime. These issues are analyzed in the following sections.

4.1 Aperture requirements

The upgraded VELO detector [8, 9] has a minimal distance of nominally 3.5 mm from the beam axis, an aperture that is considered safe in the expected (HL-)LHC conditions of Run 3 and Run 4 [run34]. For the proposed implementation of the SMOG2 storage cell, it is worth noting that, assuming a symmetric envelope with respect to the IP, the downstream edge of the VELO always approaches the beams more closely than the upstream part of the storage cell, as depicted in Fig. 8.
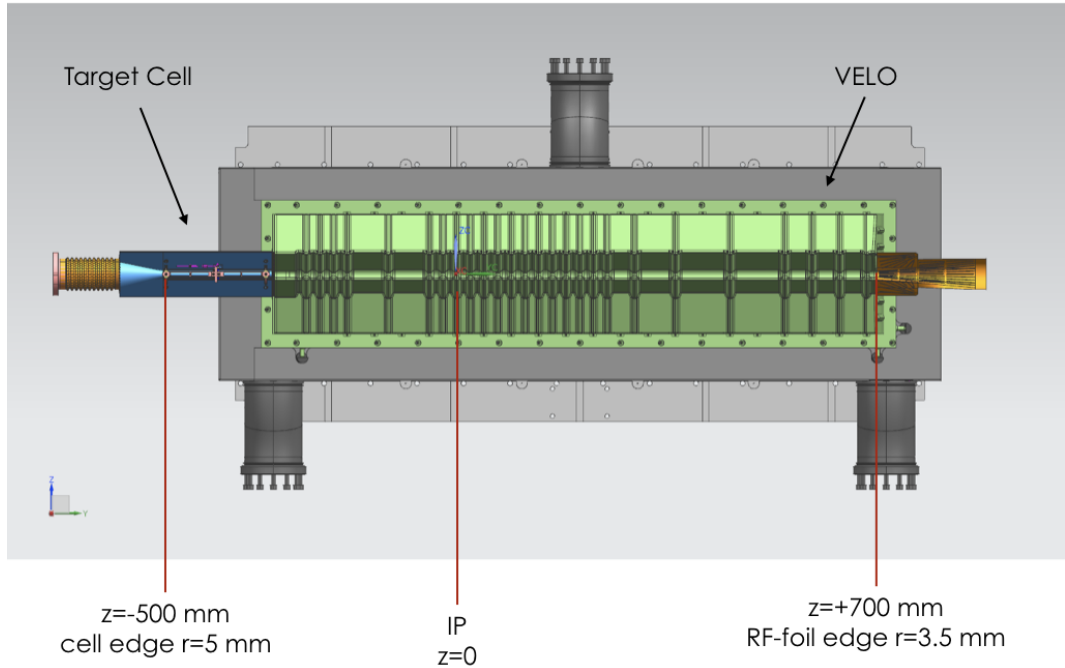

Figure 8: Side view of the SMOG2+VELO system. The coordinate with respect to the IP and the radius if the extreme apertures are reported. The beam enters from the left side.

A front view of the VELO area alone is shown in Fig. 9 (left), while the configuration with the target cell installed, and in open position, is shown in Fig. 9 (right). A circle with a radius of 50 mm has been drawn in order to visualize the maximum required aperture of the LHC during injection. By comparing the two figures, it is clear that the target walls are away from the beam and do not exceed the VELO minimum distance from the beam.
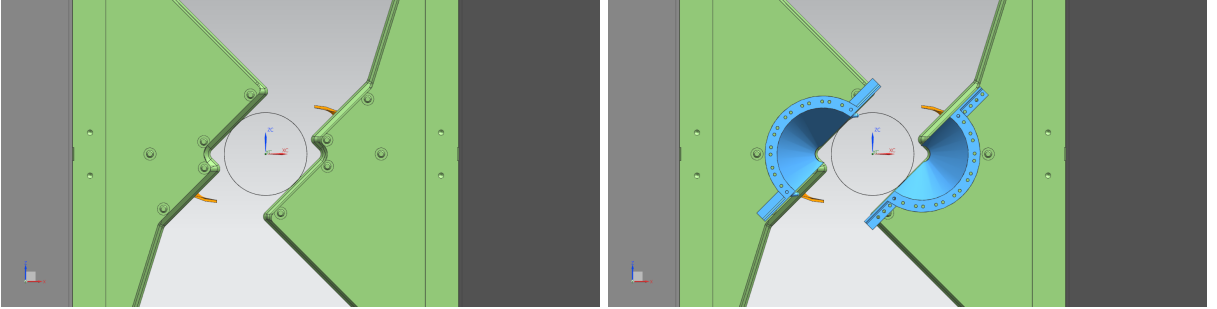

Figure 9: Front view of the VELO area alone (left) and with the target cell, in open position, installed. The circle (r=50 mm) represents the maximum transverse size of the beam during injection and tuning.

A more detailed estimate of the allowed aperture for the storage cells has been performed in Ref. [12]. Several effects were accounted for, including the transverse offset imposed by the beam crossing configuration, waist shift, beta-beating and the expected orbit shift during the physics fill. Furthermore, several machine configurations were studied, with baseline optics as well as more pushed values of β^*, both horizontal and vertical crossing configuration, and also special runs like β^*-leveling, ion runs and Van der Meer scans setup. The studies show that the minimum allowed aperture over the longitudinal range of the SMOG2 storage cell is imposed by the van der Meer scan configuration and amounts to 3 mm (when correctly assuming that the SC is centered around the closed orbit at every fill). This value does not include the SC's mechanical precision and stability. Given that the SC aperture will be 5 mm, there is ample space to accommodate these tolerances with a good margin. The results as function of the distance from the IP are summarized in Fig.10.

4.2 Impedance and beam stability

Bunched beams with 40 MHz bunch frequency and high bunch charge represent strong sources of electromagnetic fields. The general rules of guiding these beams safely are: (i) to surround them with conducting surfaces that vary as smoothly as possible in cross section in order to keep the RF field close to the beams, and (ii) to avoid excitation of cavity-like structures or other resonating systems. The side view of the system of WFS, to be installed inside the VELO vessel, is shown in Fig. 11. The beam relevant for the fixed–target measurements enters from the left (upstream) and passes through the flexible openable CuBe slotted tube, Fig. 19. The beam then enters the conical section of the cell and the cylindrical cell itself, Fig. 20. This part, consisting of two halves, is attached to the detector boxes with which it moves in open or closed position. A flexible CuBe electrical connection at the downstream end of the cell is provided by RF contacts, Fig. 21, fixed to the RF foil of the VELO detector. All these components constitute the system of WFS.
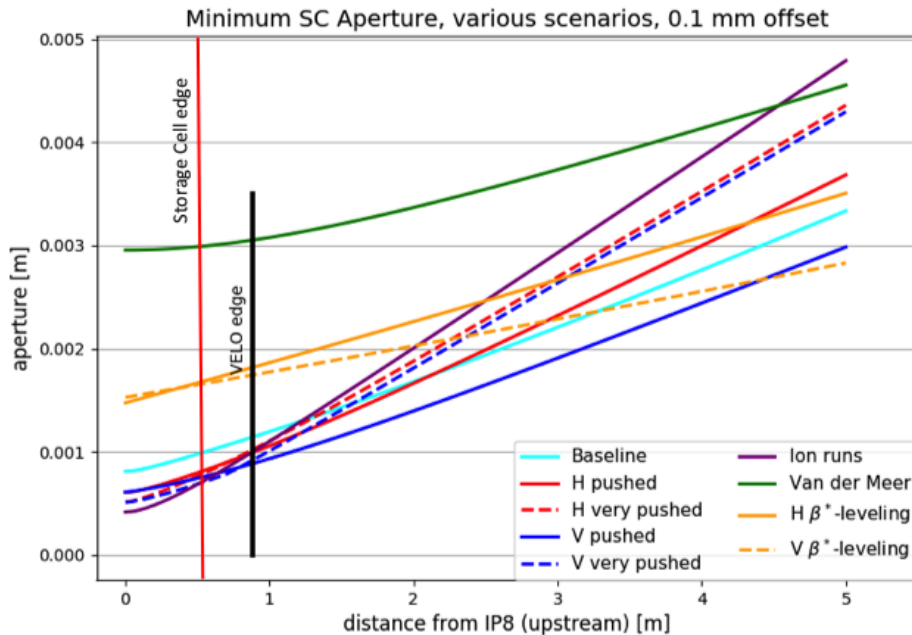
13

Figure 10: Minimum aperture for all studied scenarios. A 0.1 mm offset due to orbit drifts is assumed. The figure is from Ref.[12] while the vertical red line, representing the storage cell edge, has been added by the authors of this document.

An EM simulation campaign was started to assess the impact on the LHC of replacing a WFS on one side by the SMOG2 setup. This campaign consists of eigenmode calculations, frequency domain wire simulations, and time-domain wakefield simulations. The longitudinal and transverse wakefield simulations were benchmarked to RF measurements for the case of the VELO mockup with wire measurements [13, 14]. Results show that:

- the additional contribution to the low frequency broadband impedance due to the SMOG2 setup remains small compared to that of the VELO [16]. As a consequence, LHC longitudinal and transverse beam stability is not expected to be altered significantly by the addition of the SMOG2 setup (replacing the VELO WFS upstream);

- there is no indication that the addition of the SMOG2 setup alters longitudinal and transverse resonant modes significantly in both open and closed positions (see Fig. 12 and 13 for longitudinal impedance from simulated wire measurements) [15];

- with or without the SMOG2 setup, the local power loss could reach up to ~ 1.5 kW if the worst mode (~ 380 MHz, Rs ~ 1.5 kOhm) is hit by one the main spectral lines of the HL-LHC beam (2748 bunches with $2.2 \cdot 10^{11}$ p/b). It should be noted that hitting that single line is a possible but statistically unlikely scenario. However hitting one of the many modes above this frequency is much more likely, and would yield a power loss of the order
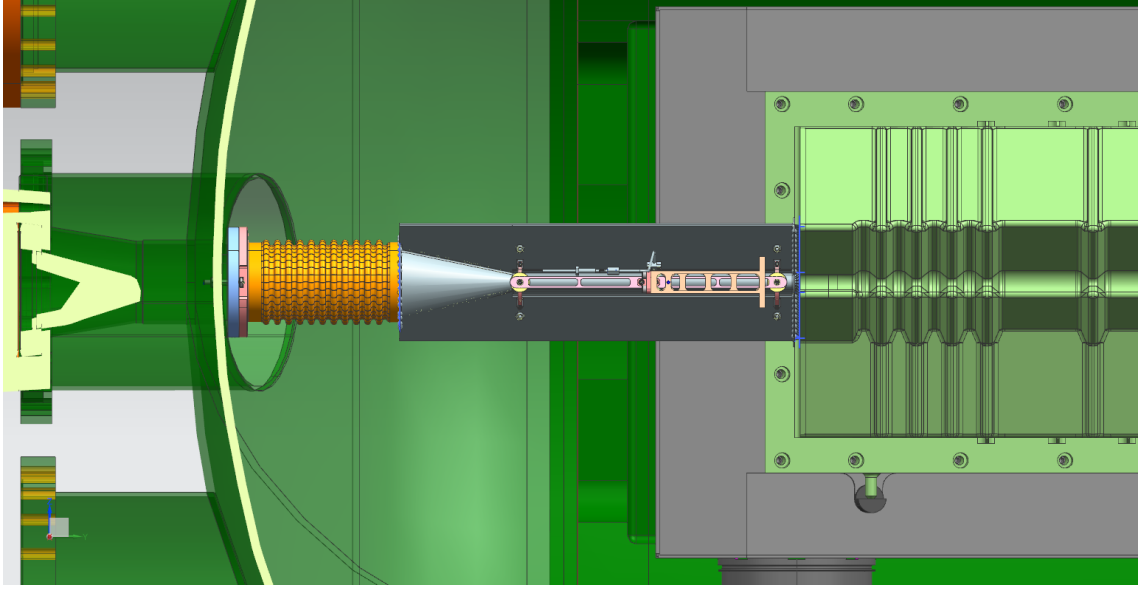
Figure 11: Side view of the storage cell inside the VELO vessel.

of 350 W. The mechanical design of the SMOG2 setup, as for the rest of the VELO, should therefore account for that possibility, and temperature monitoring is recommended. It is worth to mention that the situation in the open position is essentially the same as in Run2 (apart from the beams, which will have higher intensity) and that the 350 W are expected to be dissipated mostly in the sturdy (bakeable) vacuum vessel. Detailed simulations on heat dissipation into the open SMOG2 system have been recently reported by [17]. In the extremely pessimistic[2] case, resonance shifts of $\pm$ 20 MHz, 14 W into the whole cell have been estimated. They can increase up to a factor 4 in case the two beams create the same, simultaneous, dissipation. No resonant heating into the closed cell is to be expected.

- at the occasion of the test bench RF measurements with the VELO mockup, the situation got much worse when the wakefield suppressor shape was altered by a bridge breaking. It is therefore very important that the mechanical structure is robust enough to keep the design shape throughout LHC operation.

An estimation of the heating power dissipated in the Al cell walls, by wall currents, has been performed using [18]:

$$P_{cell} = \frac{1.226 \cdot c}{4\pi^2 \ b \ \sigma_z^{3/2}} \sqrt{\frac{Z_0}{2\sigma_c}} \frac{\bar{I}^2}{N_b \ f_r} \tag{4}$$

where c is the speed of light, $b = 5$ mm (minimum cell radius), $\sigma_z = 7.6$ cm (bunch-length), $Z_0 = 377$ Ω (vacuum impedance), $\sigma_c = 3.8 \cdot 10^7 (\Omega$ m$)^{-1}$ (Al conductivity), $N_b = 2800$ (number of bunches), $f_r = 11245$ Hz (revolution frequency) and $\bar{I} = 1.0$ A (average beam current). The resulting overall heating power for two colliding beams is $P_{cell} \simeq 4.0$ W, which will have a negligible effect on the cell stability and temperature. A precise measurement of the temperature

---

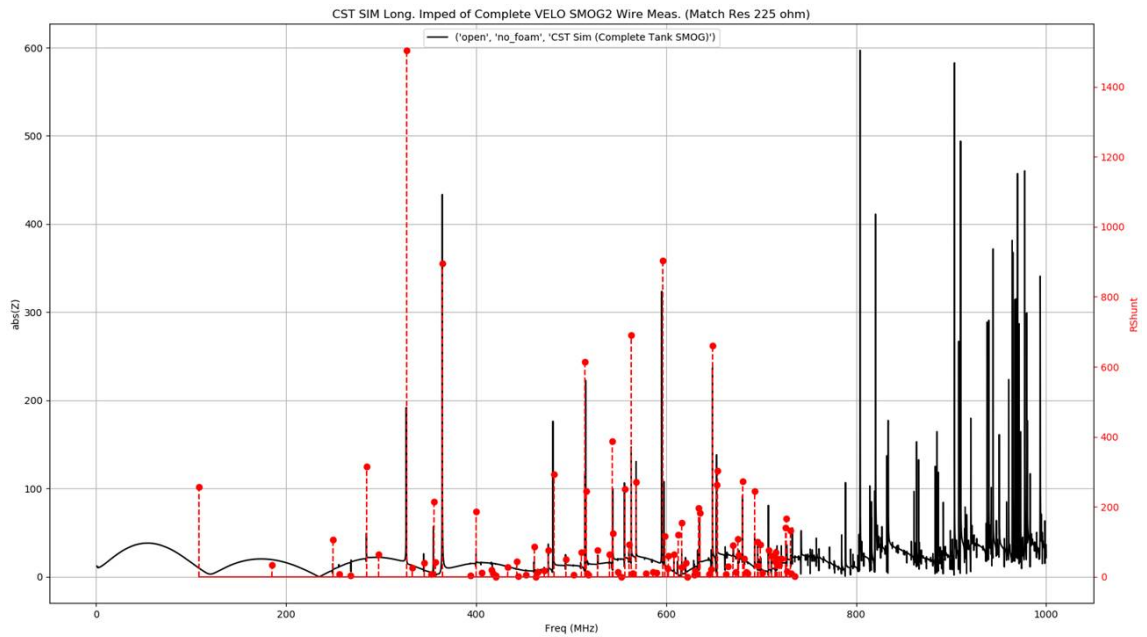[2]definition given by the LHC Impedance Group

Figure 12: Simulations of the VELO with SMOG2 and downstream wakefield suppressor (Open Position): eigenmode simulations (red dots) and longitudinal impedance from simulated wire measurements (black line), Ref. [15].
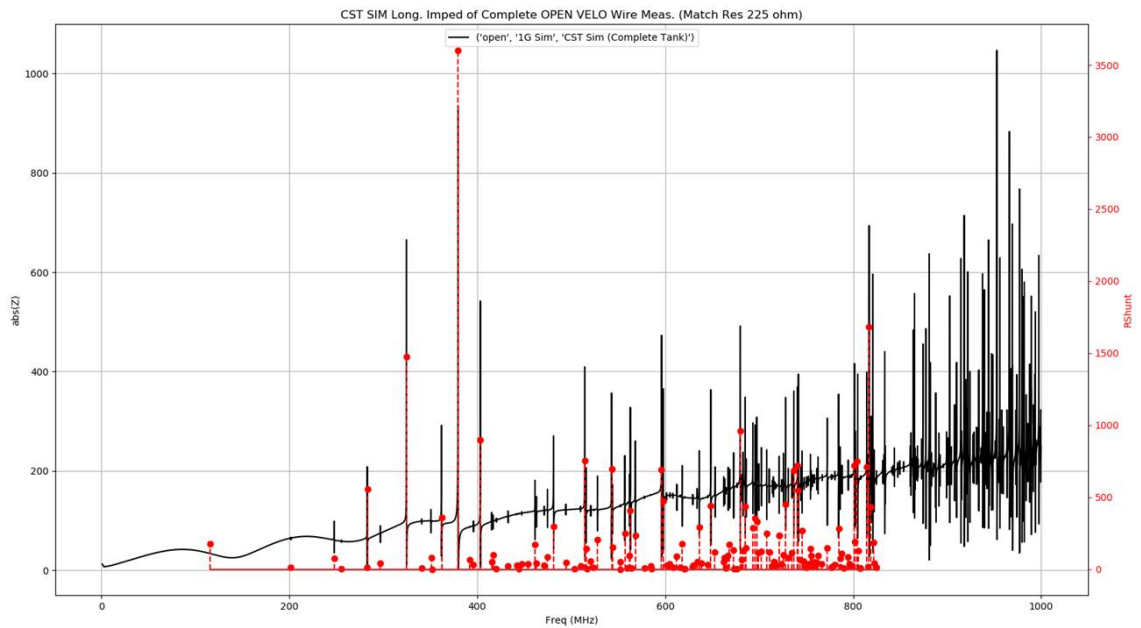

Figure 13: Simulations of the VELO without SMOG2, with upstream and downstream wakefield suppressors (Open Position): eigenmode simulations (red dots) and longitudinal impedance from simulated wire measurements (black line), Ref. [15].

is anyway mandatory for the calculation of the target density. As explained later in details, sensors attached to the cell center are foreseen to monitor the cell temperature.

4.3 Equilibrium cell temperature by radiation cooling for heat input P_i

If a resonant mode exists that could steadily be excited by the beam and dissipate substantial heat into the storage cell, then a storage cell temperature increase could be observed. It is estimated that, in the open-detector configuration, about 5% of up to 350 W will be absorbed by the cell structure, i.e. up to 14 W. Together with the losses by wall currents we assume that about $P_i = 9$ W of thermal power will be dissipated in every cell half. In case of good thermal contact of the cell suspension (i.e. to the VELO detector box) this would keep the cell temperature close to the ambient temperature T_2. Here we assume, in a worst-case scenario, that there is no thermal contact and the cell will rise in temperature until the full power is radiated-off by the cell surface, leading to an equilibrium temperature T_1. A rough estimate can be performed, using the Stefan-Boltzmann radiation law $P_{rad} = \epsilon \sigma T^4 A$ with the emissivity assumed to be $\epsilon = 1$ (black coating), $\sigma = 5.67 \cdot 10^{-8}$ $W/m^2 K^4$, and the area of one cell half to be $A \simeq 300$ cm^2. We assume that the "cold" surface, the VELO vessel, at T_2 covers the full solid angle. The net heat flow is $dQ_{12}/dt = C_{12}\sigma A(T_1^4 - T_2^4)$. We put the geometry factor $C_{12} = 1$ due to the assumption about the solid angle. Then we can write for the steady state condition with $T_1 = T_2 + \Delta T$:

$$[T_2 + \Delta T]^4 = T_2^4 + \frac{9 \ W}{(0.03 \ m^2 \ 5.67 \cdot 10^{-8} \ W \ m^{-2} \ K^{-4})} = 1.34 \cdot 10^{10} K^4 \tag{5}$$

and with $T_2 = 300$ K resulting in $\Delta T = 40$ K.

As a result, we conclude that the cell stabilizes at a temperature about 40 deg above that of the VELO vessel just by radiation cooling, and that the cell system will not be affected in such a thermal run-away situation.

4.4 Electron cloud and ions build-up effects

Electron Cloud (EC) effects are observed in accelerators with positive particles. Slow electrons produced by various ionization processes are trapped near the beam. They are accelerated by the bunches towards the walls of the beam chamber, producing secondary electrons, which may lead to an avalanche multiplication effect forming dense EC's. As a result, transverse instabilities may occur, i.e. transverse oscillations with exponential growth, which can cause beam losses. An elevated residual gas pressure favours EC formation, as well as high Secondary Electron Yield (SEY) from the chamber walls. For this reason, surfaces exposed to the LHC beams need to have a low enough SEY. For SMOG2 this can be achieved using a surface coating. Two possible choices have been considered:

- Non-Evaporable Getter (NEG),

- Amorphous Carbon (a-C).

NEG coating is excluded for the inner surface of the storage cell because of its pumping action on some of the gases, which would - apart from causing uncertainties in the determination of the target density - result in embrittlement and possible disintegration of the coating. This leads to

the conclusion that a-C is the only viable solution to suppress the formation of electron clouds. It is foreseen to coat with a-C all inner surfaces of the SMOG2 system. At first, the coating procedure has to be tested in laboratory in collaboration with the CERN coating experts for the development of the optimum procedures of surface preparation and application of a-C coating. It is important to mention that a-C coating is already applied in accelerator sections at CERN (e.g. at the SPS and at the vacuum pilot sector of the LHC A5L8).

Even in the absence of electron multipacting, the interaction of the beam with large gas densities can induce beam instabilities due to the ionization of the gas molecules. This effect was observed in the LHC and in particular in the 16L2 cell of the LHC arc, where an accidental gas inlet took place in 2017. It should be noted that:

- The integrated gas densities foreseen for SMOG2 are at least two orders of magnitude lower than in the 16L2 case (where the gas was generated by sublimation of flakes released off the pipe);

- The β function at the SMOG2 location is at least one order of magnitude smaller than in the LHC arcs;

In a recent study, the conditions of EC formation in the LHCb gas and the onset of fast beam instabilities have been analyzed in more detail [19]. The authors conclude that for SMOG2 gas densities of 10^{13} cm^{-3}, strong EC build-up is not expected at SEY up to 2.3. A lower SEY would give an extra margin on the beam stability. For gas densities 2–3 orders of magnitude higher, well above the design values, the heat loads could be very high even at low SEY. Nevertheless, during the commissioning of the device it is recommended to increase the gas density gradually while closely monitoring its impact on the beam quality.

4.5 Impact on beam lifetime

When target gas is injected, an additional beam-loss mechanism occurs, due to the beam-gas collisions. The impact on the beam lifetime can be described in terms of the total beam-gas cross section σ_{loss} and the expected luminosity L:

$$\tau_{loss}^{-1} = \frac{dN_{beam}}{dt} \cdot \frac{1}{N_{beam}} = \frac{1}{N_{beam}} \cdot L \cdot \sigma_{loss}, \tag{6}$$

with $L = N_{beam} \cdot f_{rev} \cdot \theta$. One then obtains:

$$\tau_{loss} = \frac{1}{f_{rev} \cdot \theta \cdot \sigma_{loss}}. \tag{7}$$

Some relevant results are presented in Tab. 2. In all practical cases, the resulting beam partial lifetime largely exceeds the typical duration of a fill. For instance, for the case of an Argon target, one obtains about 97 days for pAr, and 22 days for PbAr.

5 Storage Cell Design

Views of the storage cell arrangement inside the VELO vessel are presented in Fig. 11 and Fig. 14. The cell has a length of 20 cm, a diameter of 10 mm (in closed position) and consists of 200 μm. It consists of two halves that are moved together with the two halves of the VELO box (Fig. 14

Table 2:   Selected results for relative beam loss and beam life time reduction.

Beam	Target Gas	σ_{loss} (barn)	τ_{loss} (days)	Relative loss in 10 h
p	H	0.05	2060	0.02 %
p	Ar	1.04	97	0.4 %
Pb	Ar	4.63	22	1.9 %

and Fig. 15). Electrical connectivity at the upstream and downstream ends are assured by CuBe wake-field suppressors. The gas is injected in the cell center by means of a thin capillary.
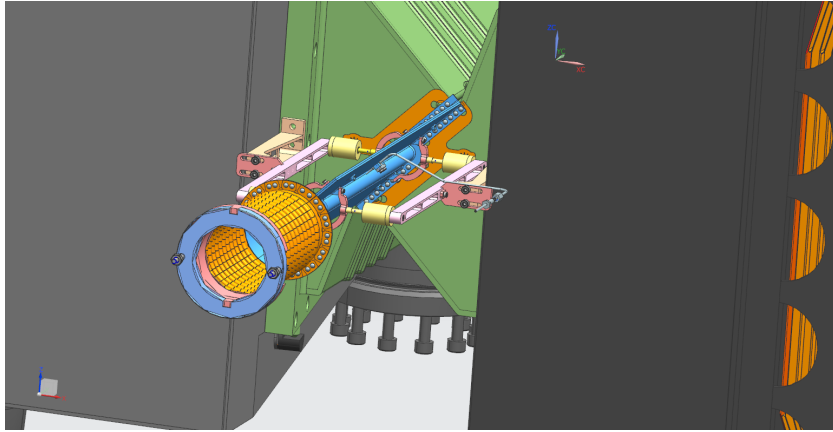

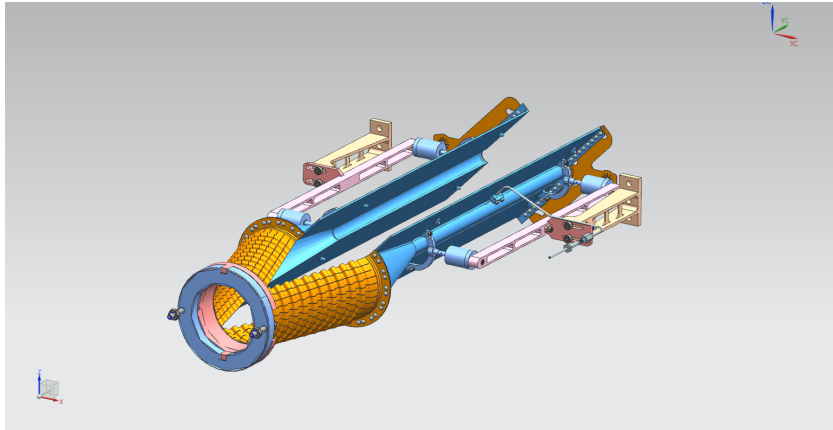Figure 14:   View of the target cell, in the closed position, attached to the RF flange.

Figure 15:   Target cell in the open position.

5.1   Cell design and construction

As explained above in details, the cell system is composed by a cylindrical WFS, a conical shape that allows for a smooth transition from the larger diameter of the upstream beam pipe (56 mm)

to the smaller diameter of the cell tube (10 mm), an open-ended tube with wings and a contact piece of the WFS system which connects to the VELO detector box. The extreme flexible parts are made by CuBe, while the rigid parts are entirely made of 99.5% pure Aluminum.

To fulfill the design requirements, the cell is realized by a milling machine starting from an Al block. The accuracy of the machining is of the order of 20 μm. Before completing the realization procedure, the cell is heat-treated at 290 °C for one hour to allow for stress release. This temperature is the best compromise to prevent deformations in the machining: a lower temperature does not provide a significant improvement, while a higher temperature causes greater material softening and less effective prevention of the deformation in the machining. A reduction of the distortion is also obtained by the use of a small milling tool diameter and by high cutting speed. A dedicated vacuum plate will be used to keep the half cell fixed in place during the operations, Fig. 16.

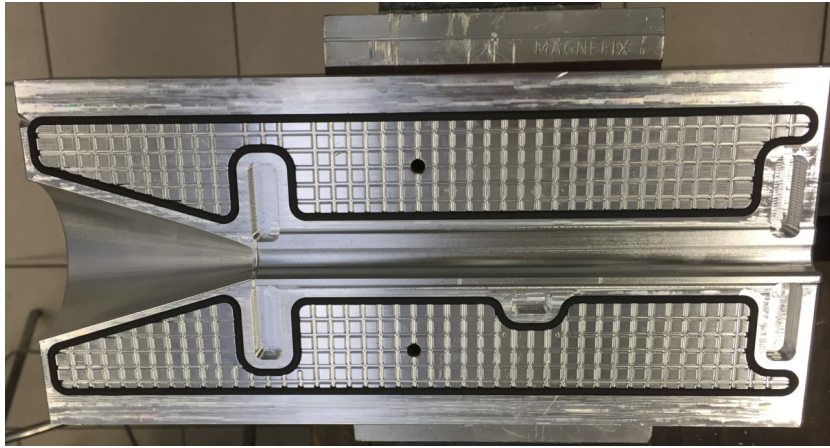All screws will be silver coated and perforated in compliance with the standards for systems in vacuum.

Figure 16:   Vacuum plate for keeping the cell in place during the flattening of the surfaces.

5.2   Support and moving system

The cell opens and closes together with the VELO detector boxes to which it is rigidly mounted by two cantilevers screwed to the frame of the VELO RF foil; the threaded holes are prepared by the NIKHEF group (Fig. 14). The VELO design foresees the possibility to operate the detector at a closed position which is slightly retracted relative to the nominal closed position to take into account possible inaccuracies of the detector RF boxes or positions (at the level of ∼0.1 mm). To compensate for this uncertainty, one half is rigidly fixed to the detector box, while the other has a certain flexibility to move. This is performed by a spring system (Fig. 17) that allows the half cell with flexible mount to assume the final closed-position, defined by the rigid half. The AISI304 spring is realized by a special tool that allows the definition of the pitch and the diameter. A hole on the cylinder containing the spring assures evacuation during the pump–down of the VELO vessel. The spring system allows to reach the cell nominal closing position even if the VELO halves are not completely closed, within a range of 0.5 mm. A prototype of the cell with its supports is shown in Fig. 18.
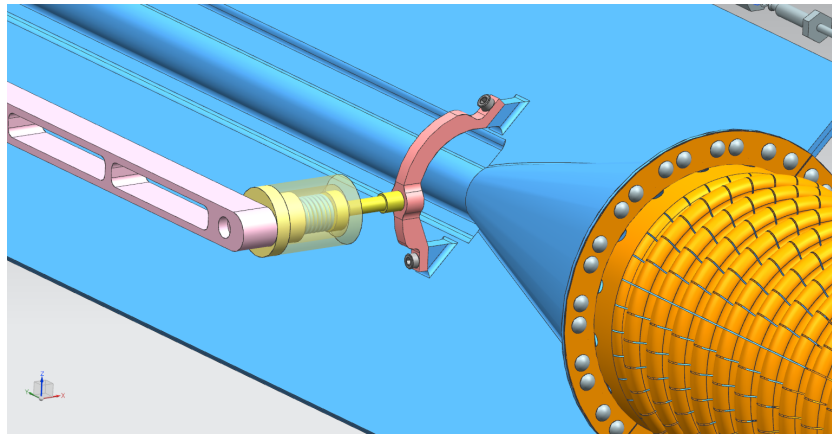
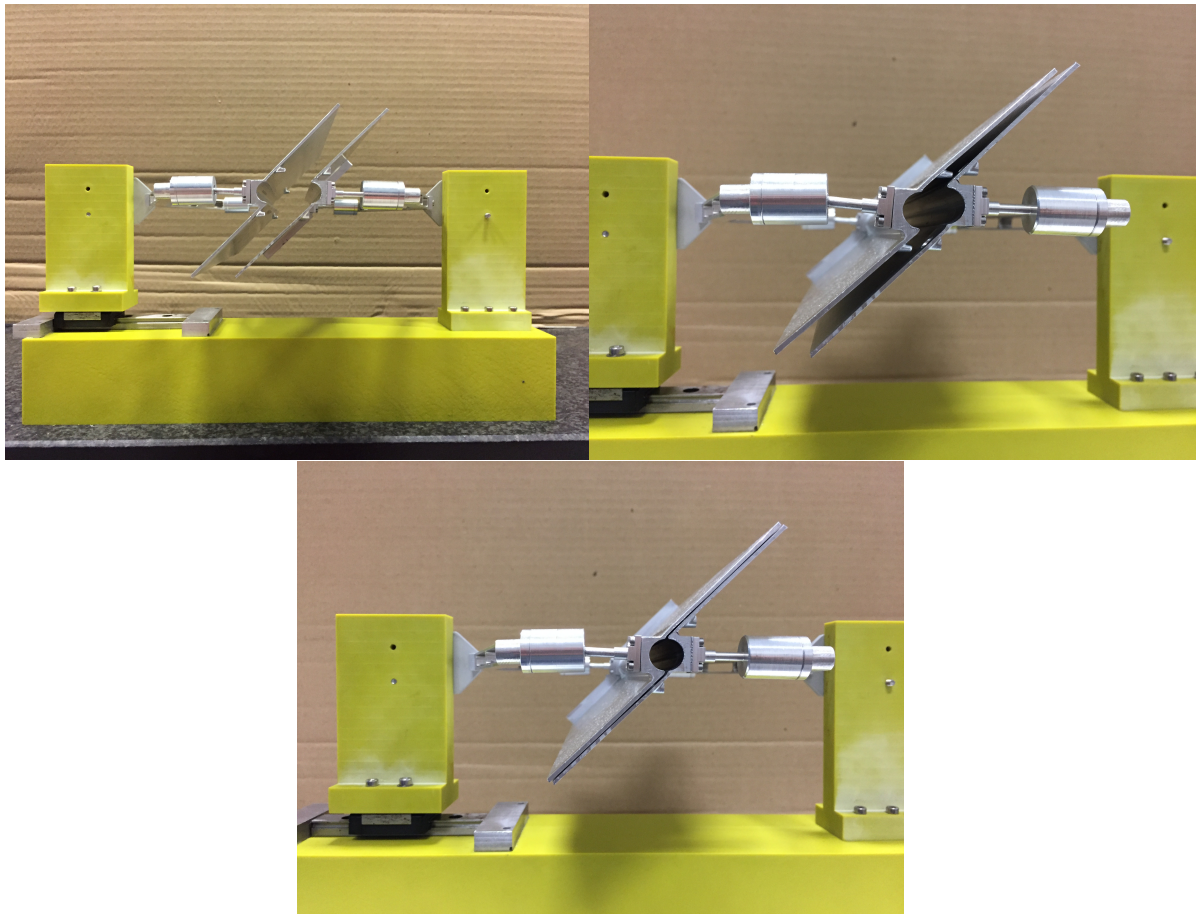Figure 17: Details of the spring system mounted on the floating half cell.

Figure 18: Cell prototype in open position (top left), engaging (top right), and closed position (bottom) . This prototype (old version) was employed to optimize the cell closing mechanism.

5.3 System of wake field suppressors

The upstream WFS (see Fig. 19) connects to the beam pipe. It consists of strips of two CuBe foils acting as a spring, forming two flexible half-tubes able to follow the motion of the cell. A smooth adaptation from the diameter of the cell to the one of the beam pipe is provided by a conical transition at the upstream end of the cell, Fig. 20. This rigid conical structure has the additional advantage of allowing the WFS to move without significant deformations. A number of pumping holes in the conical structure will be implemented in order to improve pumping of the gas flow from the storage cell to the VELO vacuum pumps (and thus reducing the flow to the LHC beam pipe). Simulations are ongoing to define the minimum hole area required for this purpose, while maintaining good RF shielding and mirror image conduction. Its edge will be fixed to the cell by aluminum rivets. This edge sits in between the cell connecting surface and a CuBe cover (0.2 mm thick). The sandwich and the pressure of the rivets will increase the electrical contact and withstand the temperature variation.

The downstream contact piece of the WFS system connects the cell to the RF foil of the VELO detector in analogue way to the existing WFS and it is mechanically connected to the cell following the same technique of the upstream WFS. The part connected to the cell RF foil will be joined to the WFS?s springs by silver brazing procedure, Fig. 21. The functionality of the WFS will be proven with a fatigue test with a number of cycles of the order of 15000[3]. The experimental setup already used for the first version of a WFS prototype is shown in Fig. 22.

5.4 Timeline for prototypes

In order to produce the first prototype according to the final and approved drawings, the realization of the tools needed for cell construction is of about three months. An additional month must be added for the assembly and the functionality tests.

5.5 Gas inlet and temperature sensors

For the gas inlet and temperature sensors we will use a CF 200 flange on the top of the VELO vessel, just above the cell position, which is now closed with a viewport. Here it is possible to put a transition of the same standard equipped with flanges on the side. This has the advantage to keep the visibility through the viewport in case of need.

The gas is injected into the storage cell through a female VCR 1/4" connector, at the air side, to a male VCR 1/8" connector, at vacuum side, welded on a DN16CF flange (or bigger). A standard 1/8"[4] capillary of 0.72 mm i.d. and 3.2 mm o.d., terminated with a female VCR 1/8", will be connected to the vacuum feedthrough. The capillary will follow the required path in the VELO vessel and come close to the cell and be terminated with a M3 bolt junction, as shown in Fig. 23. The last section of the capillary consists of Al and ends with a conical shape, with an inner diameter 0.3÷0.5 mm, which sticks on a hole made on the center of the cell, without intruding beyond the inner surface of the cel.

Very thin (0.34 mm o.d.) temperature sensors, K–type ThermoCouples (K–TCs), insulated with inconel, terminated with ceramic connector for their use in ultra high vacuum, will be

---

[3]Considering 4 cycles per day and 250 days of operation per year, this is equivalent to 15 years of working time in the experiment.
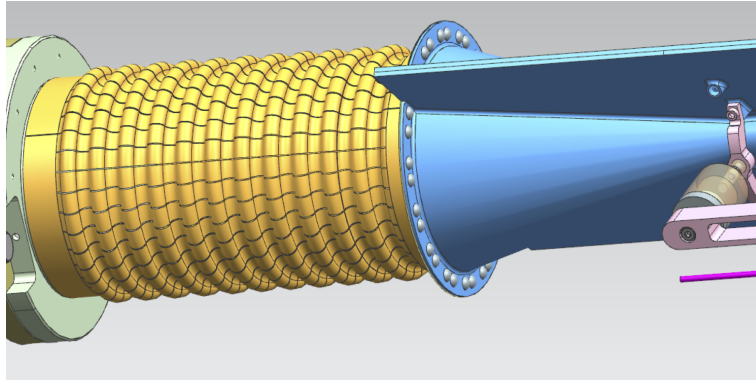
[4]Swagelock.
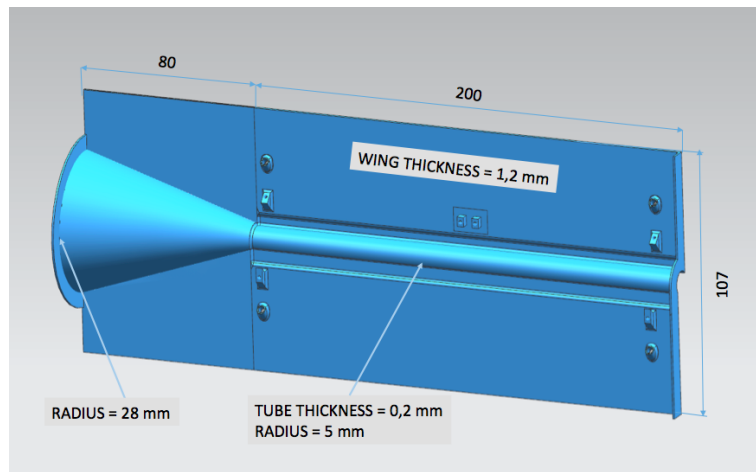
Figure 19:   Details of the upstream WFS.

Figure 20:   Details and dimensions of one half of the cell and transition cone.
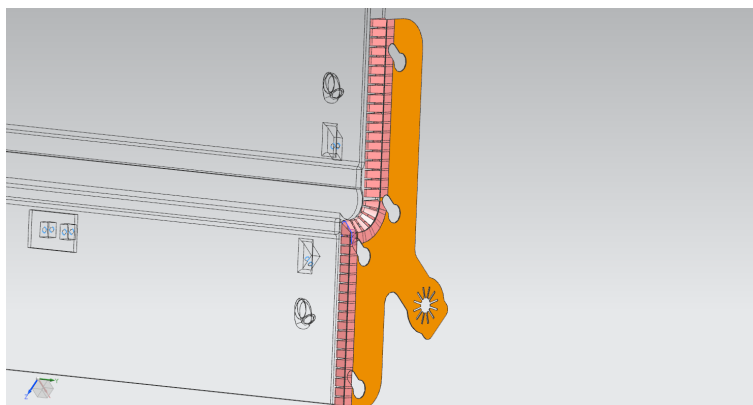

Figure 21:   Contact piece providing electrical contact from cell to the RF foil.
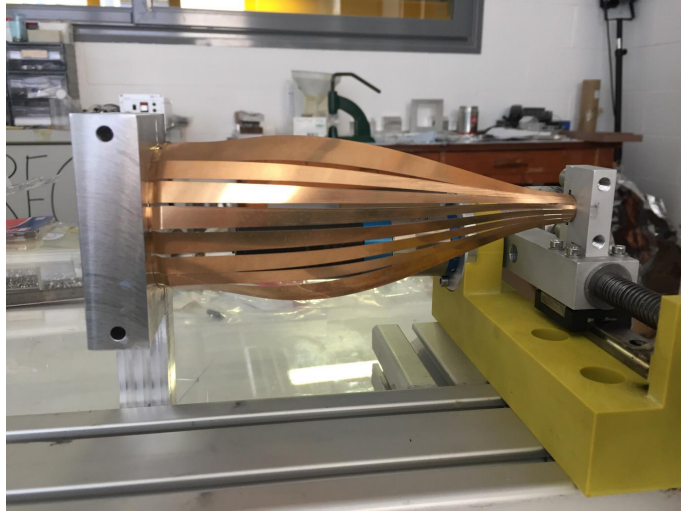
23

Figure 22: Device for the fatigue test of a WFS prototype.

connected to standard DN16CF on the side of the CF 200, where also the target feeding transition will be installed.
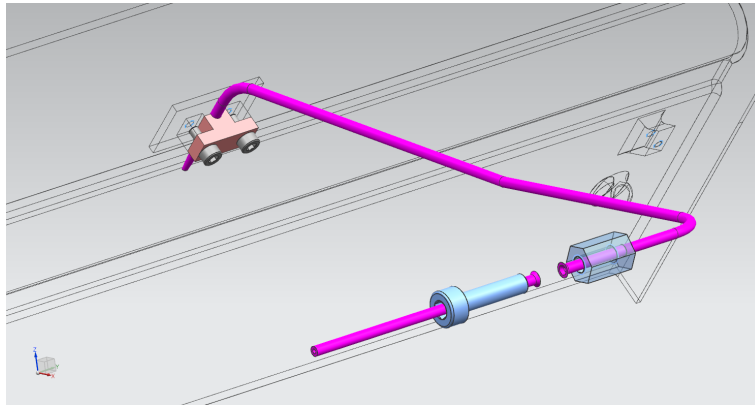

Figure 23: Preliminary sketch of the connection between the GFS system and the capillary. The aluminum capillary, at the side of the cell, has conical shape and fits in the hole at the center of the cell. The other end, passing through a nut, is properly shaped in order to ensure the sealing with the stainless tube passing through the bolt (M3 standard).

6   SMOG2 Gas Feed System

The SMOG apparatus is equipped with a gas feed system, shown in Fig. 2, which allows to injects gas into the VELO vessel, Fig. 5. This system has only one feed line (used for different noble gases), and cannot provide accurate determination of the injected gas flow rate Q.

For SMOG2 a new GFS, schematically shown in Fig. 24, has been designed. This system includes an additional feed line directly into the cell center via a capillary, Fig. 23. The amount

of gas injected can be accurately measured in order to precisely compute the target densities from the cell geometry and temperature.

Beyond the constraints requested by LHC and LHCb, the scheme shown in Fig. 24 is a well established system, operated by the proponents in previous experiments [20, 21].

6.1 Overview
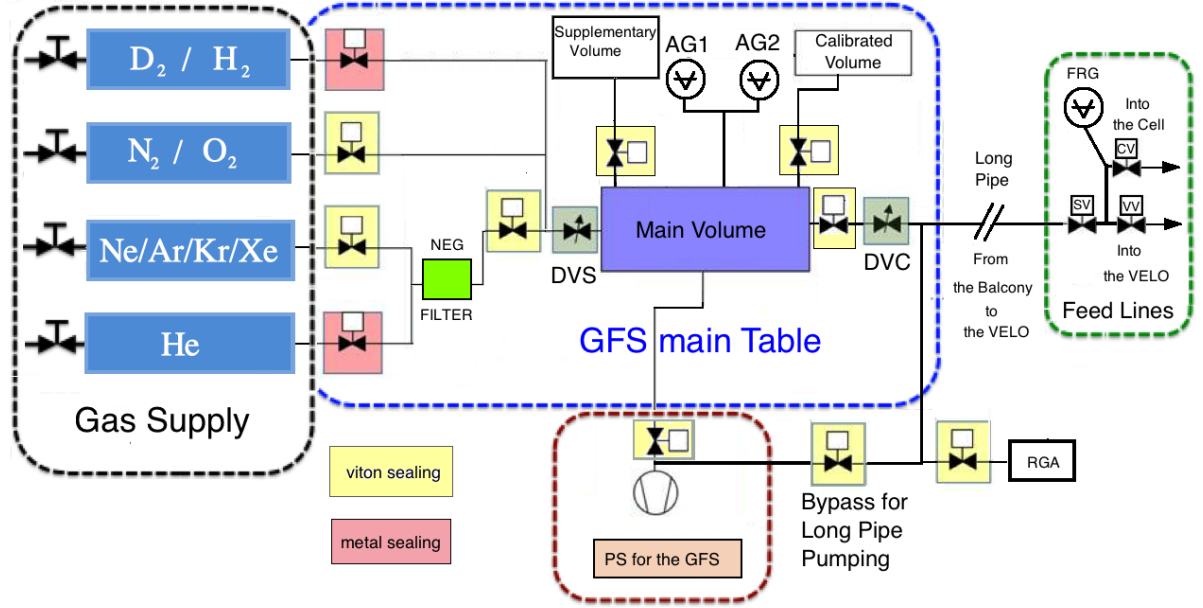
The system consists of four assembly groups, Fig. 24.

Figure 24: The four assembly groups of the SMOG2 Gas Feed System: (i) GFS Main Table, (ii) Gas Supply with reservoirs, (iii) Pumping Station (PS) for the GFS, and (iv) Feed Lines. The pressure gauges are labelled AG1 (Absolute Gauge 1), AG2 (Absolute Gauge 2). The two dosing valves are labelled DVS (Dosing Valve for Stable pressure in the injection volume) and DVC (Dosing Valve for setting the Conductance). The Feeding Connections include the feeding into the VELO vessel and into the storage cell. The corresponding valves are labelled CV (Cell Valve), VV (VELO Valve) and SV (Safety Valve). A Full Range Gauge (FRG) monitors the pressure upstream of the last valves for feeding into the vessel (VV) and into the Cell (VC). A RGA with restriction and PS will be employed to analyze the composition of the injected gas (see Sect. 6.4). The exact location is under discussion.

(i) – GFS Main Table: Table which hosts the main components for the injection of calibrated gas flow (volumes, gauges, and electro–pneumatic valves), to be located on the balcony at the P8 cavern;

(ii) – Gas Supply: Following the requirements imposed by the CERN vacuum group and the LHCb safety rules, the gas supply is provided via reservoirs filled at a pressure lower than 2.5 bar, the maximum value allowed on the DVS dosing valve for stable pressure conditions. Each reservoir consists of a cylindrical tube of i.d. 63 mm which can be extended up to 1100 mm in length (and with an i.d. 100 mm for the extension). The maximum volume obtainable is about 8.6 l, corresponding to about 17 bar l, filling the reservoir at a pressure of 2 bar. At the highest gas flow rate of $3.4 \cdot 10^{-4}$ mbar l/s used in [6], the reservoir will safely ensure a duration of more than one year. The possibility to install a set of gas bottles outside the restricted area (A side) is also envisaged.

(iii) – Pumping Station (PS) for GFS : The GFS pumping station consists of a 70 l/s turbo pump and a dry backing pump.

(iv) – Feed Lines: They include two feedthroughs. The first one is used for feeding the gas into the VELO vessel. This could be the same as installed at present between TP 301 and GV 302 (see Fig. 5). The second one, with the capillary for feeding the gas into the storage cell, will be placed on the top upstream flange of the VELO vessel.

6.2 Theory of SMOG2 operation

As described in Sect. 3.1, the gas flow rate Q is related to the particle intensity $I = dN/dt$ in Eq. (1). If the system is at temperature T one has:

$$Q \stackrel{\text{def}}{=} \frac{d\,(pV)}{dt} = \frac{dN}{dt}kT \; , \tag{8}$$

at constant temperature T one has and where k is the Boltzmann constant.

The SMOG2 GFS, shown in Fig. 24, allows to inject a well know gas flow rate Q according to:

$$Q = \Delta p \; C_{inj} \approx p_{inj}C_{inj} \; , \tag{9}$$

where $\Delta p = p_{inj} - p_{cell} \approx p_{inj}$, and p_{inj} and p_{cell} are the pressure in the injection volume V_{inj} and in the cell itself. Here, C_{inj} denotes the conductance of the whole feed line.

The pressure p_{inj} can be measured by membrane/capacitance gauges with a relative accuracy of 0.15 %. As they are thermo-stabilized[5], the measurement is not affected by temperature variations.

The conductance C_{inj} of the whole feed line, from the injection volume to the center of the cell or to the VELO vessel, determines the time dependence of the injection pressure p_{inj}:

$$p_{inj}(t) = p_{inj}(0)\mathrm{e}^{-\frac{C_{inj}}{V_{inj}}t} \; . \tag{10}$$

In the viscous regime, in which the GFS works, the conductance C_{inj} is pressure–dependent. Therefore, it has to be determined at the actual working pressure p_{inj}.

A direct way to determine the flow gas rate Q in Eq. (8), is to measure the derivative of the pressure during flow calibration, knowing the volume V_{inj}:

$$Q = -\frac{dp_{inj}}{dt}V_{inj} \; . \tag{11}$$

---

[5]The temperature of the gauge is stabilized at 40 °C.

It should be noted that this is the basis of gas flow rate measurements employed in the GFS.

For a precise determination of Q the volume V_{inj} has to be measured accurately. The volume V_{inj} can be given by V_{main} (Fig. 24), for low Q_{inj}s, or $V_{main} + V_{suppl}$ for high Q, where V_{suppl} is a supplementary volume. Therefore the volumes have to be determined precisely. This can be done by means of a calibrated volume V_{cal}. The size of the unknown volume V_{main} can be determined just by gas expansion from V_{cal} to $V_{main} + V_{cal}$ and measuring the resulting (lower) pressure.

Assuming an attainable precision of 0.1 % in the measurement of the V_{cal}, and considering the reading uncertainty of 0.15 % in the pressure measurements, one obtains an uncertainty of ≈ 0.4 % on V_{main}. This error propagates into the error of Q leading to an uncertainty of less than 1 %. Using a similar GFS, an overall uncertainty of a few percent has been achieved at HERMES [22], and confirmed in other systems, too.

6.3   Technical realization

The implementation of the GFS scheme is under study in cooperation with the CERN – TE/VSC–ICM vacuum group. The technical realization of the GFS main table is in progress, and a preliminary design is shown in Fig. 25. The system is based on precise absolute (baratron = capacitance/membrane) gauges. They usually cover four decades of pressure reading. Therefore, in order to have a wide operative pressure range for commissioning and operation, two of these (thermos-stabilized) gauges will be installed:

(i) Absolute Gauge 1 (AG1), which covers a pressure range from 1100 to 0.1 mbar[6],

(ii) Absolute Gauge 2 (AG2), which covers the range from 1.1 to 10^{-4} mbar[7].

The absolute gauges will measure and monitor the pressure p_{inj} in the injection volume determining the stability of the injected flow, necessary for a stable target density. The latter is maintained by setting a nominal pressure and keeping it constant by means of a thermo–regulated valve[8], the Dosing Valve for Stable gas pressure (DVS) Fig. 24. One of the two absolute gauges (AG1 and AG2) in Fig. 24 can be selected in order to automatically tune the actual pressure to the set one. The controller[9] can regulate the opening of the valve by reading directly the gauge pressure or by acquiring the output from a multigauge controller[10].

After stabilizing p_{inj}, another thermo–regulated valve, the DVC in Fig. 24, will be set at a proper value depending on the gas type and the gas flow rate chosen (Q_{inj}). The DVC can be regarded as a tuneable conductance in series with a fixed one, represented by the feeding tube and the capillary, thus allowing for tuning the whole C_{inj}.

The connection of the GFS to the VELO (long pipe shown in Fig. 24) will be performed by a 10 mm i.d. pipe with a length of 15-20 m. A complete mapping of the path has already been planned and will be performed as soon as the LS2 will start.

The size of the volumes (V_{main}, V_{cal}, etc.) employed in the GFS must be optimized in dedicated test bench measurements in order to obtain the best overall performance in the different ranges of operation, based on the experience of the HERMES and PAX systems (see Ref. [22]).

---

[6]Pfeiffer CMR271 gauge.

[7]Pfeiffer CMR274 gauge.

[8]Pfeiffers EVR 116.

[9]Pfeiffers RVC 300 controller.

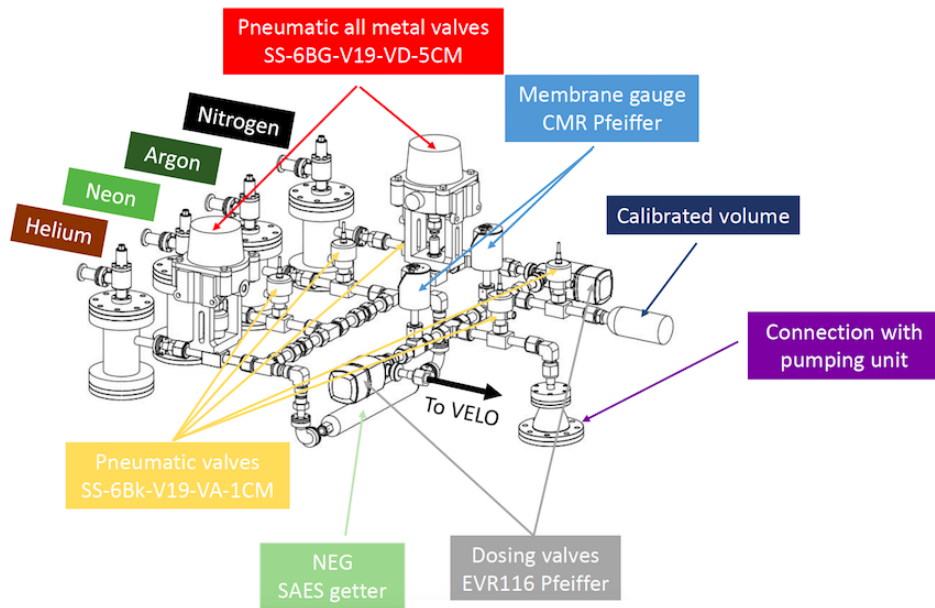[10] Pfeiffers TPG 256 A multigauge controller.

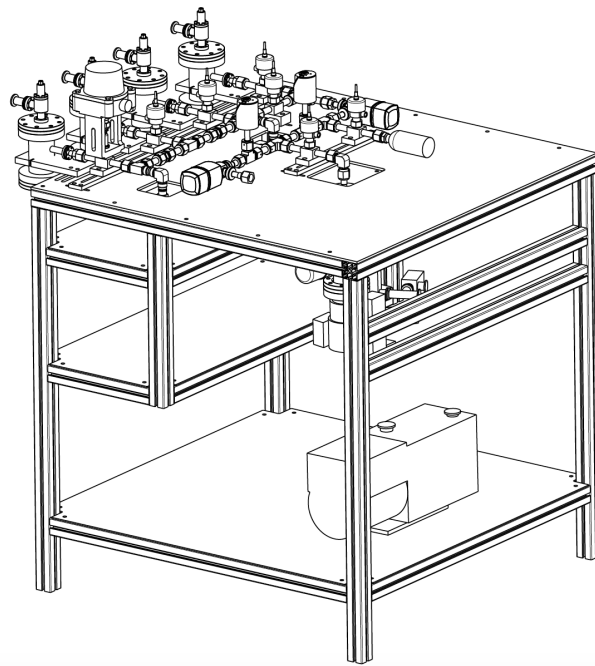Figure 25: Top: the stand hosting the GFS main table to be located on the balcony of the P8 cavern. Bottom: details of the GFS main table including the Pumping Stations (PS). (Courtesy of CERN-TE/VSC-ICM).

6.4 Operation and control

A preliminary setup of the proposed GFS is shown in Fig. 25. The GFS operation will remain under the CERN – TE/VSC–ICM control and responsibility. The components are piloted by

the following electronic modules:

RVC 300 (Pfeiffer – Balzers) for the Dosing Valve DSV: This module hosts baratron, and controls automatically the dosing valve DVS[11] in PID logic, in order to keep the actual pressure equal to the set one. The opening of the valve can be controlled by a 0–10 VDC. The module can be remotely piloted with the RS232/RS485 communication port and standard. In order to exploit the whole range provided by the gauges, a range switch is required in order to select the proper one, according to the working conditions.

RVC 300 for Dosing Valve DVC: The module controls the percentage of the opening of the DVC. The module can be remotely controlled by the standard RS232/RS485 communication port.

TPG256 (Pfeiffer – Balzers) gauge controller: The TPG 256 can read out up to six gauges: (i) the High Vacuum gauge of the PS, (ii) a Low Vacuum gauge on the inlet of the backing pump, (iii + iv) the two absolute gauges on the GFS, and (v) the FRG on the VELO feeding, leaving one channel open. In addition, the module can provide eight relays controlled by programmable set-points on the read-out of any gauge hosted by the module. The module provides also six analogue outputs 0–10 VDC. One of the channels can be selected by a switch for serving as input into the RVC 300 of the DSV stability control valve.

VCM (Swagelock) digital valve controller: The Digital Valve Control Module (VCM) can operate up to six Swagelock pneumatic valves. The module also monitors the status of the valves and can be remotely controlled by PLC modules.

PS controller: It will follow the existing system at CERN.

We can distinguish the following working conditions, which will require the proper setting from the slow control. Below only a brief summary is provided. It will be detailed and agreed in future with the responsibles of the slow–control system.

Evacuation of the GFS and/or the long pipe: The PS can be employed alternatively, or simultaneously, for pumping the GFS and the long pipe.

Selecting gas: For the selection of the gas the DVS has to be completely closed, and the valves of the proper reservoir opened.

Feeding at a chosen Q: The PS is pumping on the main volume (eventually enlarged by other volumes, too). The SV, CV and VV valves are open, and the relevant injection pressure is being monitored by the FRG (see Fig. 24). At low–enough pressure in the volumes, the valve between the volumes and the DVC is opened. With the parameters for the feeding set for the RVC 300 (controlling the DVS) and the RVC 300 (controlling the DVC) the correct flow is set and the VV valve closed.

Stopping the feeding gas and preparing for evacuation: For this action, the valve between the volumes and the DVC, the CV and SV valves closed. Then the bypass is opened in order to pump down the *long pipe* and the short connection upstream of the DVC to the final pressure.

---

[11]Pfeiffers EVR 116.

Feeding a chosen pressure into the VELO vessel: This requires the same sequence used for feeding into the cell, except the fact that now it is not necessary to open the CV valve on the VELO. The setting for the RVC 300 of DVS and RVC 300 of DVC will be different, just determined by the required pressure in the vessel.

Residual Gas Analyzer: The purity of the injected gas can be determined by an RGA including a small PS. One option is to connect this unit via needle valve to the main volume, thus allowing for the analysis of the injected gas. It could also be used for other tasks on the GFS main table, like leak detection.

6.5   Commissioning and operation

The whole system can be commissioned and operated on a laboratory test bench, connected to a vacuum chamber which can mimic the VELO vessel and the proper connection between the GFS table and the feedthrough into the VELO and into the cell. The latter includes the conical end plug of the capillary, inserted and safely secured in an appropriate hole in the cell wall. The influence of the conductance of the connecting lines can be studied, together with the calibration procedures and uncertainty estimations, during laboratory tests, using the same final configuration. The working parameters set to both RVCs can be obtained recording evacuation curves and studying the reproducibility of the system in the laboratory. These measurements have to cover the required range of gas flow rate for the different gases. Once determined, they then can be used at the experimental site. The final commissioning of the system mounted on the experiment can be performed after all tests in the laboratory have been successfully completed. As already stressed, the first measurements will be the validation of the calibration curves found in the laboratory. During normal operations, recording of calibration curves is required periodically in order to test the reproducibility and the stability of the GFS.

7   Installation Procedure

Before starting with the installation procedure, the following preliminary operations are needed:

- Two cantilevers supporting the cell must be fixed on the RF foil frame. Threaded holes will allow the connection between the parts.

- Alignment: the alignment of the VELO detector box is performed acting from the sides, following a procedure developed by the LHCb Liverpool group that makes use of a module metrology jig. Concerning the storage cell, only the fixed half needs to be aligned with the VELO. A first iteration with the CERN Metrology group (EN-SMM-ESA)[12] defined the following preliminary procedure:

  - a marker referring to the module metrology jig is applied on the front region of the VELO box;
  - four reference pins are temporary applied along the wing of the fixed half of the cell;
  - the alignment is performed by referring the four pins to the marker;
  - a precision of 100 μm is obtainable by this procedure;

---

[12] Jean-Christophe Gayde and Pascal Sainvitu.

– the floating half of the cell does not need to follow the same procedure since, with its three degrees of freedom, it adapts perfectly to the fixed half.
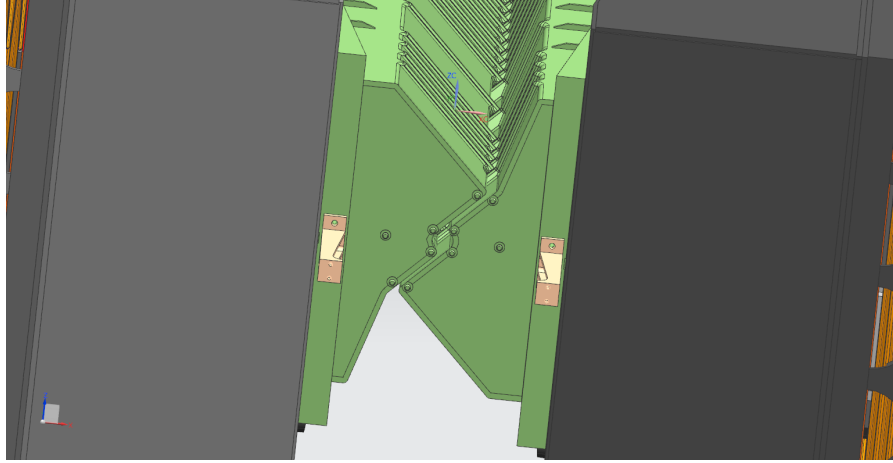

Figure 26: The two target supporting cantilevers screwed on the left and right VELO RF-flanges.

A schematic sequence of the operations required for the target installation is reported below. The points 1-6 will be performed in the laboratory at P8, on the surface, the other steps 7–10 will be done in the cavern.

1. The new VELO detector has to be completely installed, aligned and kept in open position, Fig. 27;

2. The fixed half of the cell, already equipped with the upstream and downstream WFS, is the first to be installed on the right side (C side) of the VELO. The downstream WFS slides down and engages the RF foil mushroom pins. Simultaneously, the holding support of the half storage cell has to be screwed to the supporting plate. This half is the one with the capillary for the gas injection and the thermocouples wires, Fig. 28;

3. The operation of point 2 has to be repeated on the left side (A side) of the VELO box for the floating half of the cell, Fig. 29;

4. The floating half of the cell has to move back following the yoke on the supporting plates, Fig. 30;

5. The VELO detector has to move in the closed position, Fig. 31;

6. The floating half of the cell has to be moved in the compensation position with respect to the fixed half, Fig. 32;

7. A modified spoke, designed to support the upstream WFS through a CuBe ring, will be constructed by the proponents and installed on the VELO vessel, Fig. 33. After the installation of the spoke the engaging flange will be decoupled from the lifting tool and connected to the spoke;

8. An intermediate flange for the upstream WFS connection will be fixed to the edge flange of the beam tube. Then the main flange of the VELO vessel can be closed, keeping all the service flanges open;

9. Acting from the beam tube, a special tool (Fig. 34) will connect the engaging flange of the WFS to the intermediate flange. Acting from the service flanges, the ring of the upstream WFS can be connected to the flange of the VELO vessel, Fig. 35, Fig. 36 and Fig. 37;

10. The flange on the upper and upstream part of the VELO vessel, to be used for hosting the gas feed line and the thermocouple connections, will be closed with all the internal connections assured, Fig. 38.
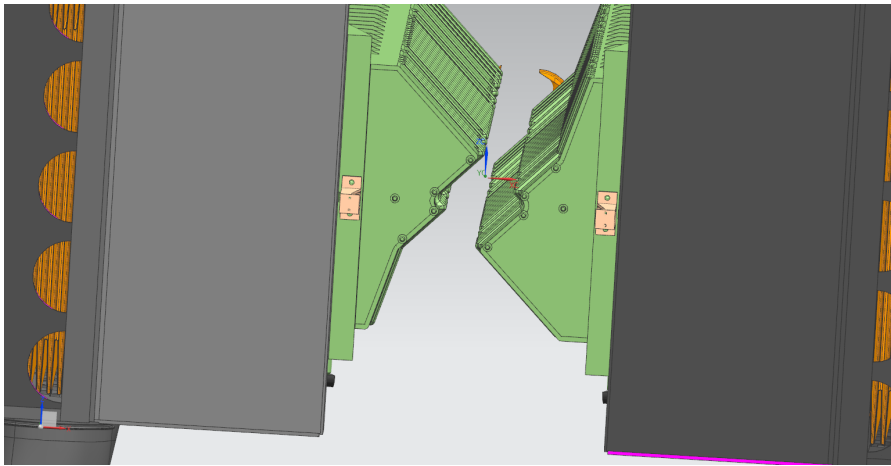

Figure 27: VELO installed and in open position. The supporting cantilevers have already been fixed to the RF-flanges.

It is worth to mention that the baseline option (i.e. without the storage cell) will be prepared by the Nikhef group in any case and it will be adopted if a show-stopping issue occurs in the finalization of the SMOG2 project.
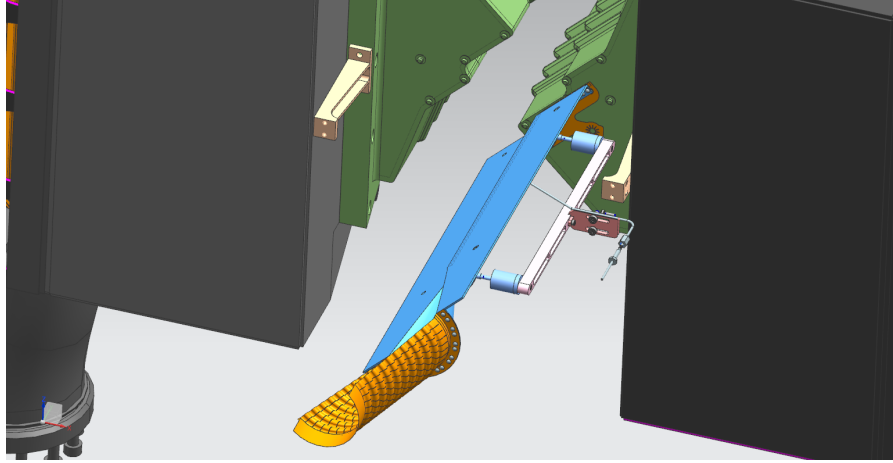
Figure 28: The right (fixed) half of the target is inserted into the mushroom pins, aligned and screwed to the cantilever.

8   GEANT4 implementation and background studies

The installation of the gas target in the upstream section of the LHCb spectrometer, always present even when the gas is not flown, adds material budget that can, in principle, increase the background seen by the sub-detectors. The background arises in the machine from proton interactions with residual gas molecules, either close to or far away from the experiment, interactions of protons with the beam collimation system and from fluxes produced by beam-beam collisions in the other LHC experiments. More specifically, the Machine Induced Background (MIB) originates from the interaction of beam protons with gas residue or material close to the beam line. For LHCb, MIB comes from two main sources:

- Beam-gas interactions in Long Straight Section (LSS) leading up to the experiment;

- Interactions with the Tertiary Collimators (TCT) located upstream on both sides of the beam pipe.

By introducing additional material close to the beam pipe it is important to evaluate the amount and characteristics of this background, not only for the design of the new target system, but also to understand possible degradation of the conditions during normal operations.

Except for the beam-gas interactions occurring inside the experiment itself, most background sources originate considerably far away from the LHCb cavern, so the data is mostly generated by non-LHCb systems [23] and then propagated to the LHCb detector simulation, using Gauss [33] (for generation and detector simulation) and Boole [34] (for the digitization).
The method adopted here follows the one described in Ref. [24, 25], where numerical analyses of the MIB at the LHC have been implemented. Each step in the chain is simulated with software specific to the task, providing input to the subsequent step through a well-defined and clear interface.

Some of the relevant parameters used for the MIB generation and simulation are reported below:
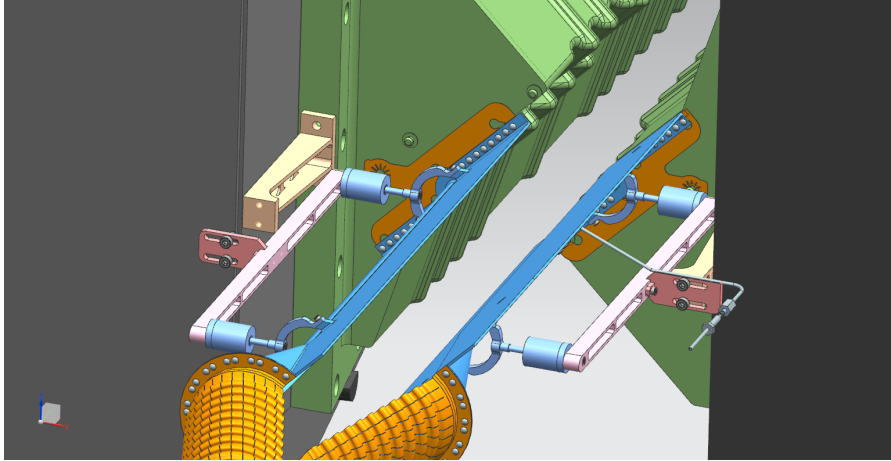
Figure 29: The left (floating) half of the target is mounted.

- Luminosity = $2 \cdot 10^{33}$ cm^{-2}s^{-1};

- Number of protons per bunch simulated N = $1.15 \cdot 10^{11}$;

- 10000 events per configuration (described below) and per MIB source.

The determination of the number of events to sample is related to the proton population in the simulated bunch, the number of passing protons represented by the source file, the number of proton losses in the file, and a scaling factor. The sum of loss weights in the file gives the amount of proton losses where at least one particle arrives at the interface plane ($z = -2.1$ m) per N passing protons. This is additionally modified by the ScalingFactor option. As a consequence, the average number of MIB events generated per bunch crossing can be calculated. In our case, the scaling factor (μ) is automatically provided in the log file generated by the code. When calculating the MIB variation due to the target, this factor is irrelevant because it cancels in the ratio. On the other hand, considering that in the simulation of the pp collisions each bunch crossing gives a single interaction, when the MIB is embedded into the pp collisions, the scaling factor is directly used to scale the MIB distributions. Considering the expected pileup of 7.6 for pp collisions in Run3, the obtained results must be considered as an upper limit.

In order to implement the target cell geometry into the LHCb one, the engineering file in the STEP-ASCII format has been converted to the GDML format in form of tassellated[13] objects, as needed by GEANT4 [26, 27, 28], Fig. 39. The structures upstream the VELO region, belonging to the nominal LHCb geometry without SMOG2, have been removed.

The simulated MIB events have been manually added to those produced in a simulation of the normal pp collider interactions. Following a procedure similar to the one described in Sect. 9, 10000 minimum-bias events have been generated for pp interactions at $\sqrt{s}$ =14 TeV for each configuration using the Monte Carlo generators EPOS+PYTHIA8 [29, 30, 31].

The VELO occupancy has been analyzed for all the configurations listed above. The VELO setup used in the simulations reported here is the one of the Run1+2, however, with smaller

---

[13]Due to the tassellated structure, the visualization of the geometry can be performed only by Geant4 and not by Root.
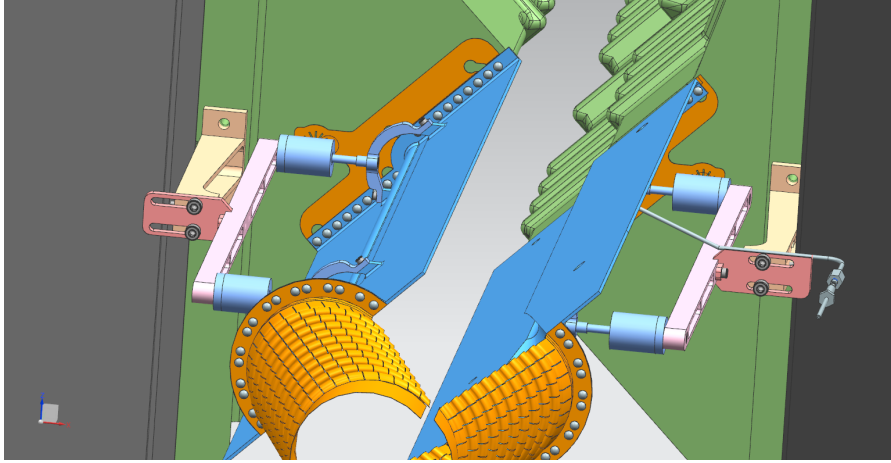
Figure 30: The left part of the cell is kept at the maximum distance by sliding the support on the fixed plate.

statistics, also the upgraded VELO has been simulated and the results are basically identical. In Fig. 40 the number of VELO clusters per event, in case of MIB in the baseline configuration (no target cell, no WFS), are shown for the TCT and LSS background sources, respectively. Figure 41 is similar to Fig. 40 but for the configuration where the storage cell has been included.

For the MIB, an additional configuration has been simulated. A full aluminum cylinder (r=20 mm and h=50 mm) has been placed instead of the target along the beam-line centered at $z = -400$ mm. This was done in order to produce an artificially large background to check that the code was working properly. As expected, the increase of the VELO hits due to the MIB increases considerably ($\sim$30%) with respect to the configuration with no cylinder.

Figure 42 shows the number of VELO clusters per event in case of normal pp collider interactions at $\sqrt{s} = 14$ TeV: (left) baseline configuration, (right) with the storage cell apparatus (but no gas into the storage cell).

The results for the various configurations are reported in Tab. 3 where the variation of the total number of VELO clusters per event is calculated with respect to the configuration with no storage cell.

We conclude that adding the storage cell system material budget in front of the LHCb detector does not change the number of VELO clusters per event in the pp collisions. The MIB alone has a variation of maximum +16%. However, when the MIB is properly scaled and embedded into the pp collisions, the effect of the storage cell is completely negligible.
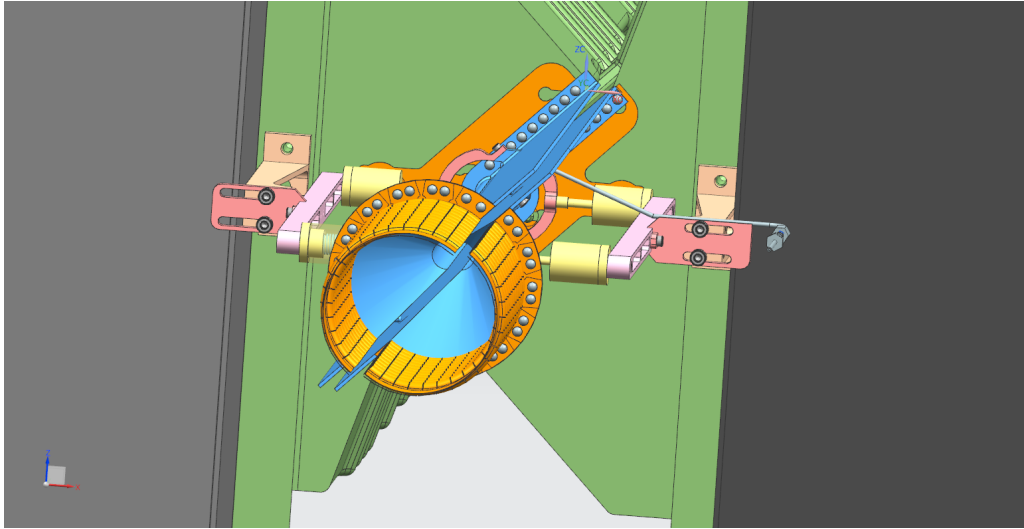
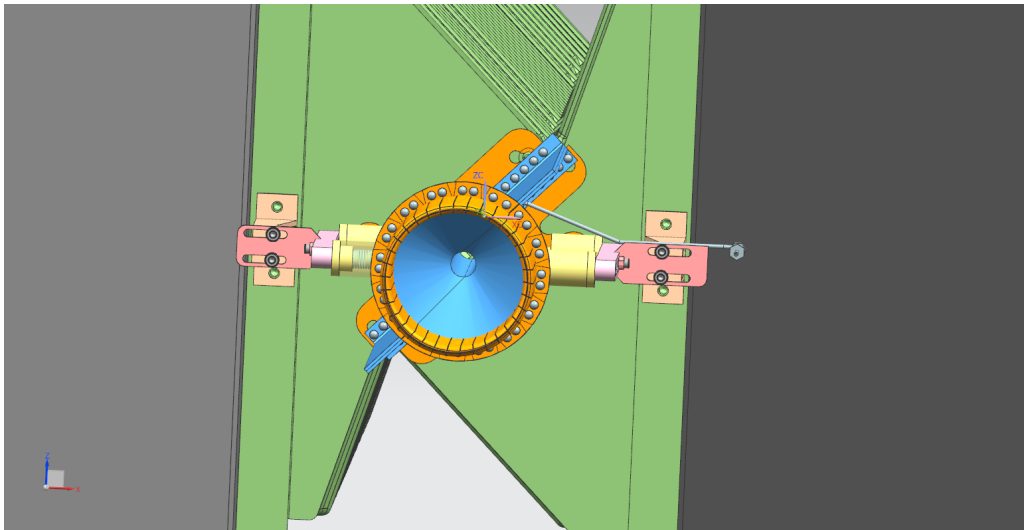Figure 31: Front view of the VELO in closed position and the target halves at maximum distance.

Figure 32: Front view of the VELO in closed position and the target halves in compensation position.
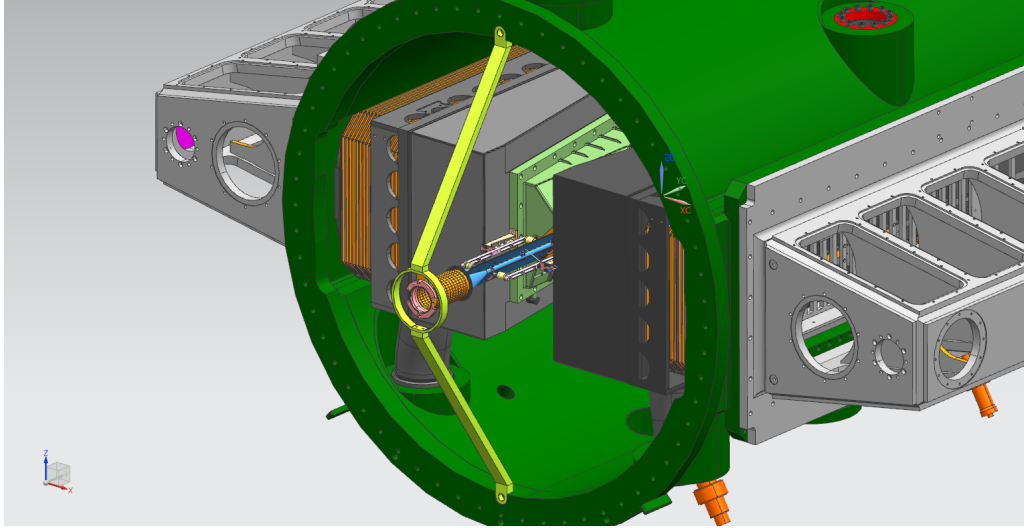
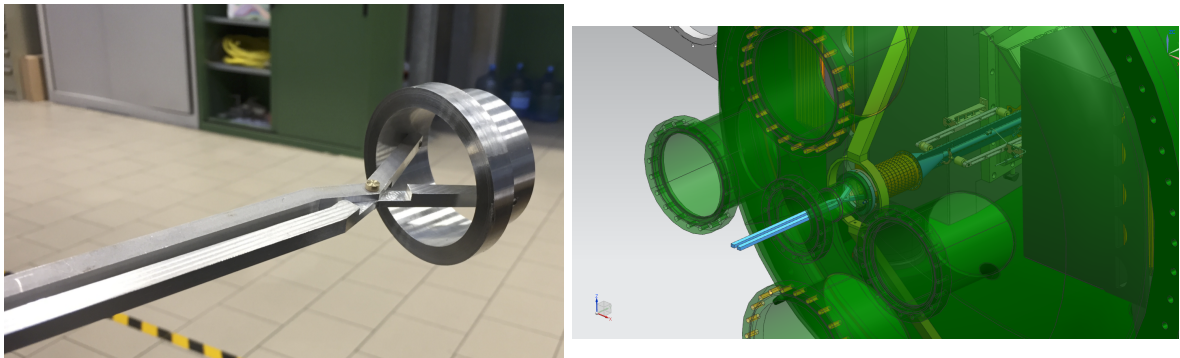Figure 33: VELO vessel with the spoke (in yellow) installed.

Figure 34: Tool used to connect the engaging flange of the WFS to the intermediate flange (left) and its use (right).
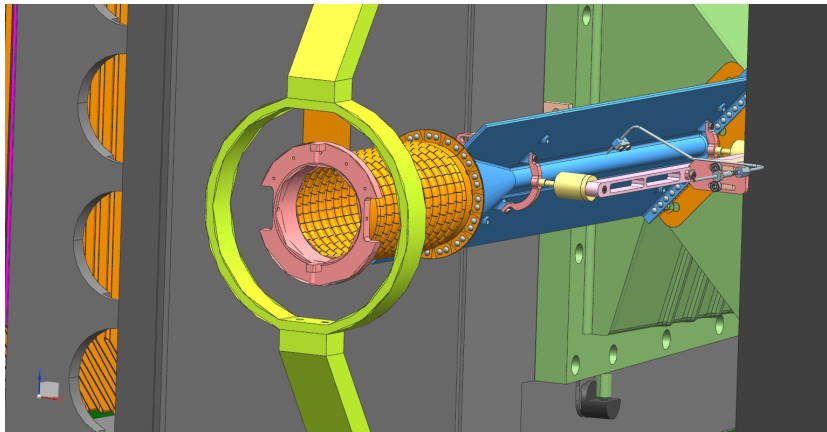
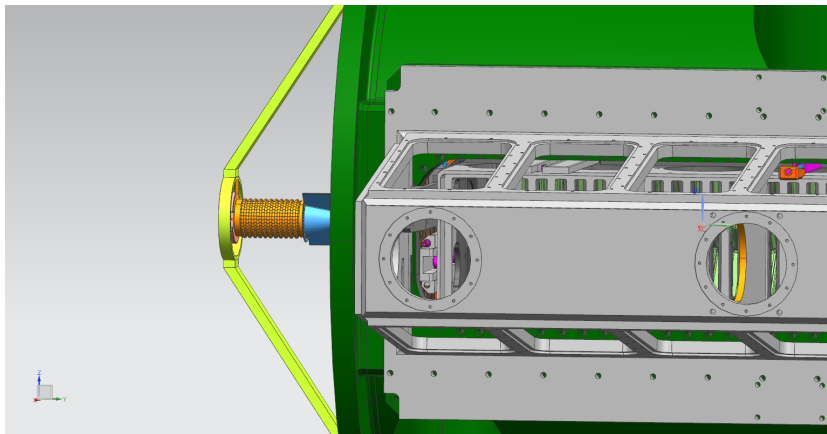Figure 35: Spoke holding the upstream end of the WFS tube.

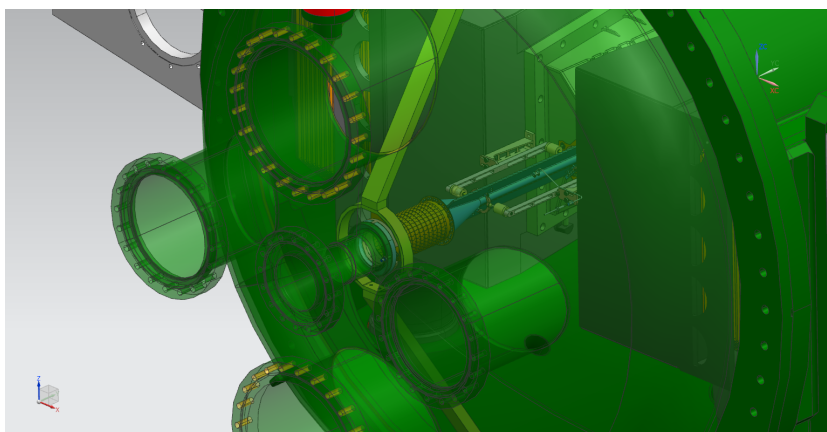Figure 36: Side view of the spoke installed in front of the WFS.

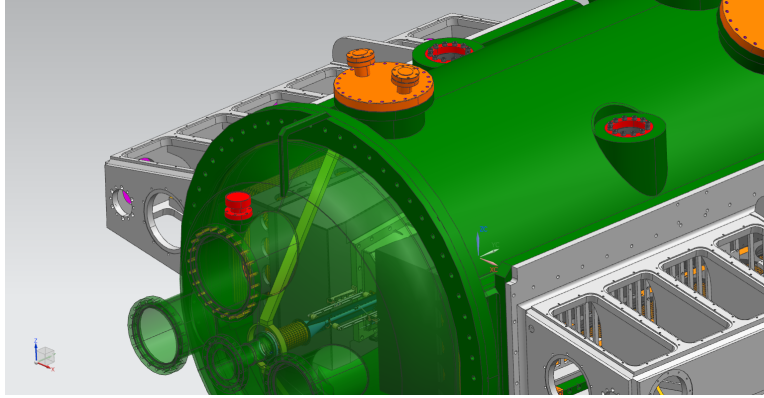Figure 37: VELO vessel closed and with the front service flanges open.

Figure 38: Flange on top of the VELO vessel to be used for the gas feed-through and thermocouples connections.

Table 3: Average VELO clusters per simulated event measured for different configurations. Here, μ represents the MIB scaling factor. The relative increase (Δ) is calculated with respect to the configuration with no storage cell.

Config.	Average VELO clusters per event						
	MIB-TCT (μ=0.0238)	MIB-LSS (μ=0.0019)	pp	pp + μ MIB	$\Delta^{MIB-TCT}$	$\Delta^{MIB-LSS}$	$\Delta^{pp+\mu MIB}$
baseline	75	481	443	446	–	–	–
with storage cell	87	506	442	445	+16.0 %	+5.2 %	0

9 Reconstruction Efficiency Studies

Simulation studies have been performed in order to compare the SMOG2 and SMOG reconstruction/selection efficiencies. The scope of these studies is to quantify the impact of the larger average distance between the VELO and the SMOG2 interaction region, as compared to the SMOG case. To this aim, estimates of the main sources of inefficiencies are evaluated for the two cases taking into account the different interaction regions along the z-axis (longitudinal position of the primary vertices, PVz) and the expected density profiles: triangular for SMOG2 (see Fig. 6) and flat for SMOG[14]. Only the differences $\Delta\varepsilon$ between the estimated efficiencies for SMOG2 and SMOG are of relevance for these studies.

[14]The expected different areal densities are not accounted for in these studies, but their effects are quantified in the scale factors reported in Table 1 and are considered in the SMOG2 projected performances reported in Section 10.
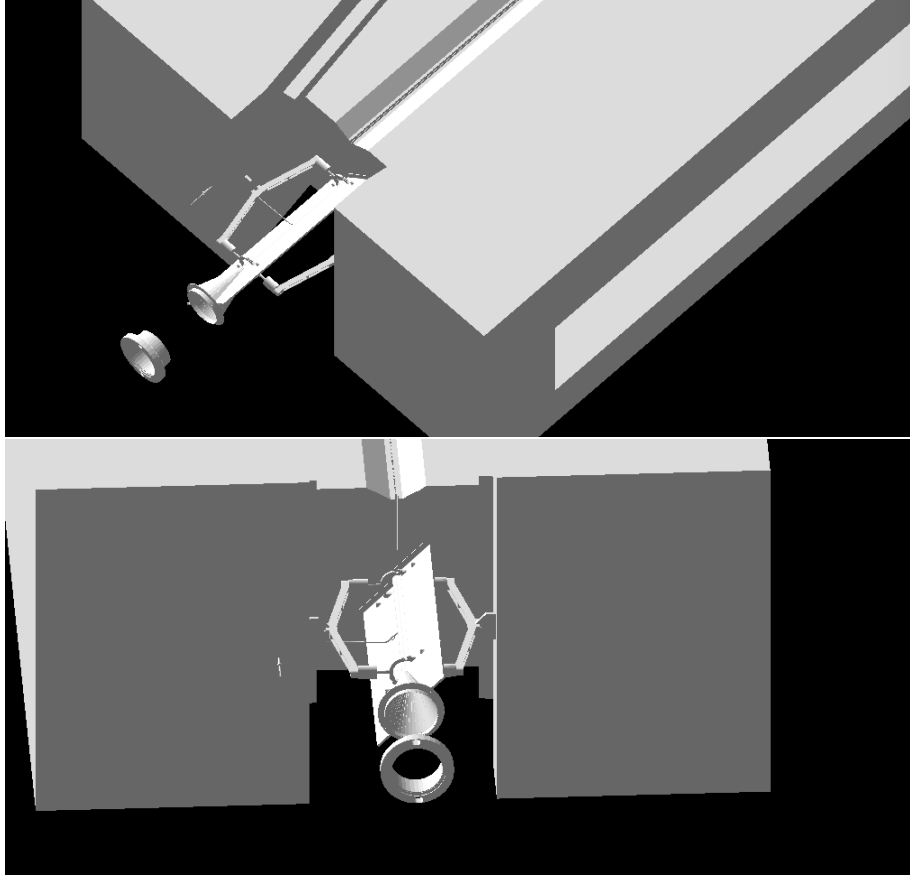
Figure 39: Geant4 visualization of the target inserted upstream the VELO box.

The interaction region used for SMOG2 corresponds to the position and length of the storage cell, whereas two different PVz intervals have been considered for SMOG (later labelled as SMOG_A and SMOG_B), corresponding to the fiducial interaction regions used in the analysis reported in [5] and [6], respectively (Fig. 43):

- SMOG2: $-500 < PVz < -300$ mm

- SMOG_A: $-200 < PVz < +200$ mm

- SMOG_B: $-700 < PVz < +100$ mm .

Two selected physics channels are considered here (both of interest for the SMOG2 physics program): inclusive production of J/ψ and D^0 mesons in fixed-target pAr collisions with a beam energy of $E_p = 7$ TeV. For the reconstruction, the following decay modes have been selected:

- $J/\psi \to \mu^+\mu^-$,

- $D^0 \to K^-\pi^+$.
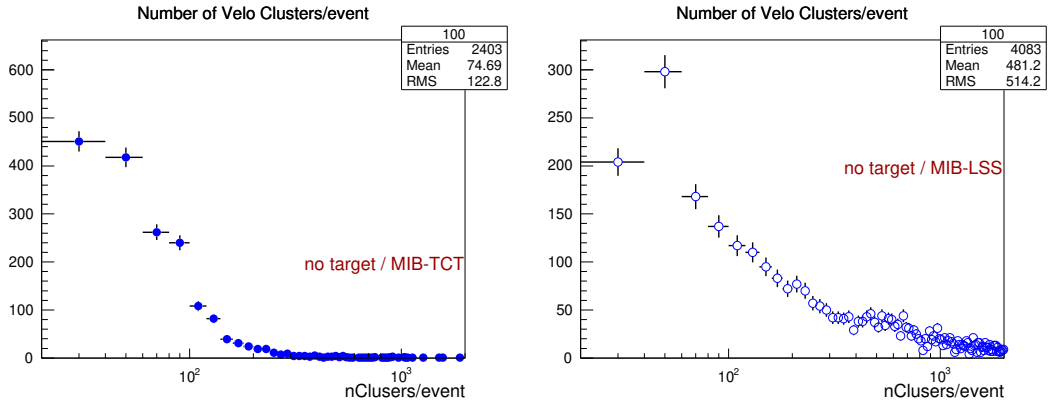
Figure 40: VELO clusters per event in case of MIB and baseline configuration (no target cell, no WFS): (left) TCT contributions, (right) LSS contributions.

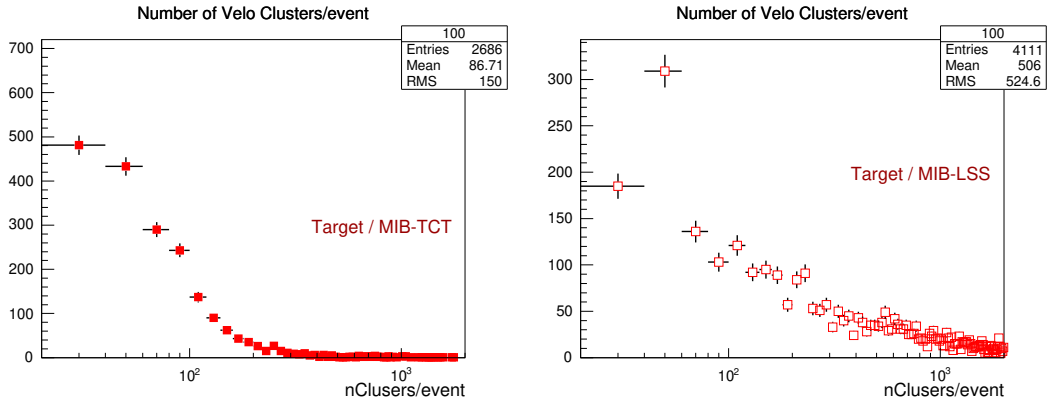Figure 41: VELO cluster per event in case of MIB with the storage cell (but no gas injected): (left) TCT contributions, (right) LSS contributions.
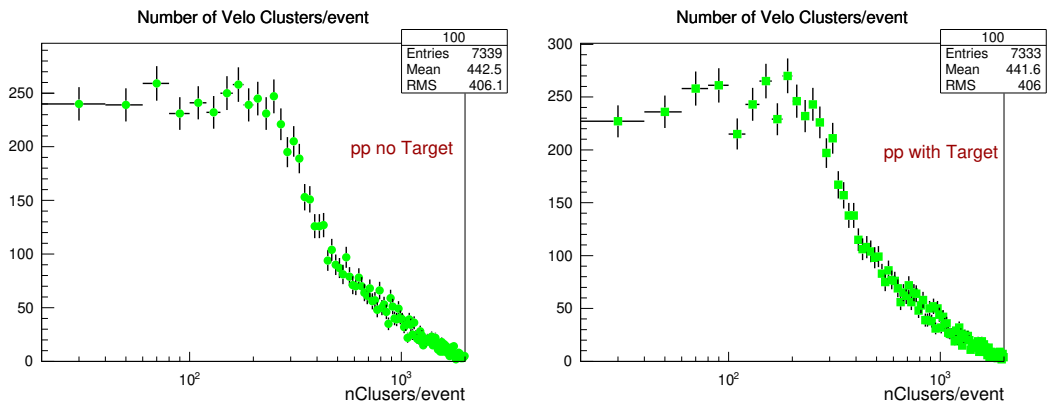

Figure 42: VELO clusters per event for pp interactions: (left) baseline configuration, (right) with the storage cell (but no gas into the storage cell).
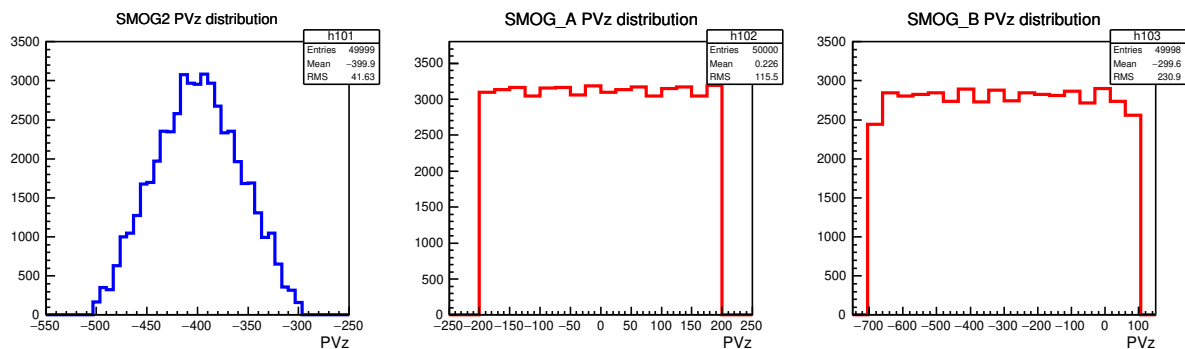
Figure 43: Primary Vertex z-distributions for SMOG2 (left), SMOG_A (center), and SMOG_B (right).

In the simulation, J/ψ and D^0 mesons are generated using PYTHIA8 [29, 30] with colliding-proton beam momenta equal to the momenta per nucleon of the beam and target. Their decays are described by EvtGen [32]. The decay daughters are then extracted and embedded into pAr minimum-bias events generated by the EPOS event generator [31]. Decays of hadronic particles generated by EPOS are also described by EvtGen. The interactions of the generated particles with the LHCb detector, and its response, are implemented using the GEANT4 toolkit [26, 27, 28]. The generation process and the interaction with the detector is performed through Gauss [33]. Digitization and trigger are accounted for with Boole [34] and Moore [35], whereas the final reconstruction and the analysis are performed with Brunel [36] and DaVinci [37], respectively. For each of the two channels, 50000 events have been generated per each target configuration.

Different sources of inefficiencies are considered, which involve both the reconstruction and the selection of the events:

- Track reconstruction;

- Acceptance cuts;

- PV reconstruction;

- PID cuts;

- Selection cuts;

- Trigger requirements.

The track reconstruction efficiency has been evaluated using the information from the MC truth, whereas all other efficiencies above are based on reconstructed and truth-matched events. The efficiency studies have been performed separately for the two physics channels and are described in the following sections.

9.1 Track reconstruction

The track-reconstruction efficiencies of the J/ψ and D^0 decay products are evaluated as the ratios between the number of reconstructed and generated tracks inside the nominal acceptance

$(1.9 < \eta < 4.9)$. The study is performed separately for the three target configurations (SMOG2, SMOG_A and SMOG_B) and the results are reported in Fig. 44 as a function of the particles pseudorapidity. A narrower pseudorapidity range is covered with SMOG2, with a lower limit around $\eta = 2.6$, against $\eta = 1.9$ for the two SMOG configurations. This is consistent with the fact that having an interaction region which is, in average, 400 mm upstream of the nominal interaction point ($z = 0$), the tracks at larger angles (smaller η) are cut out of the detector acceptance. The average estimated efficiencies are reported in Tab. 4. A drop in the efficiencies below 10 % is obtained for all cases.
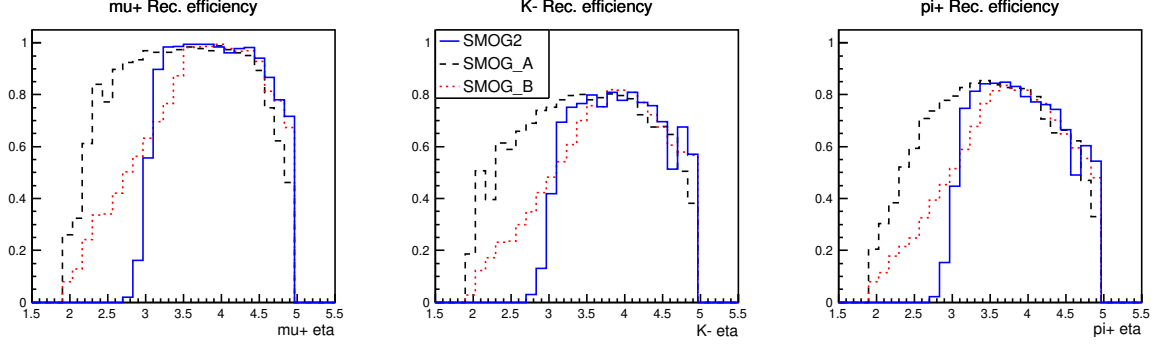

Figure 44: Track-reconstruction efficiencies as a function of pseudorapidity obtained for SMOG2 (blue full line), SMOG_A (black dashed line) and SMOG_B (red dotted line) for (from left to right): μ^+ (from J/ψ), K^- (from D^0) and π^+ (from D^0).

Table 4: Average estimated track-reconstruction efficiencies for SMOG2 and the two SMOG configurations. The last two columns report the difference between the efficiencies of SMOG2 and SMOG_A ($\Delta\varepsilon_1$) and between those of SMOG2 and SMOG_B ($\Delta\varepsilon_2$), respectively.

	Tracks reconstruction efficiencies				
	ε_{SMOG2}	ε_{SMOG_A}	ε_{SMOG_B}	$\Delta\varepsilon_1$	$\Delta\varepsilon_2$
μ^-	80%	89%	83%	$-\mathbf{9}\%$	$-\mathbf{3}\%$
μ^+	80%	87%	81%	$-\mathbf{7}\%$	$-\mathbf{1}\%$
K^-	63%	70%	65%	$-\mathbf{7}\%$	$-\mathbf{2}\%$
π^+	62%	70%	64%	$-\mathbf{8}\%$	$-\mathbf{2}\%$

9.2 Acceptance cuts

The efficiencies related to the acceptance cuts are evaluated as the ratios between the J/ψ (and D^0) yields with and without the acceptance cuts $2.0 < y_{J/\psi} < 4.6$ AND $1.9 < \eta_{\mu^\pm} < 4.9$ ($2.0 < y_{D^0} < 4.6$ AND $1.9 < \eta_{K^-,\pi^+} < 4.9$), where η and y denote the pseudorapidity and the rapidity, respectively, and by requiring truth-match (BKGCAT==0). The results are shown in Fig. 45 as a function of the J/ψ and D^0 rapidity. The average values for SMOG2 and SMOG, as well as their differences, are reported in Tab. 5.
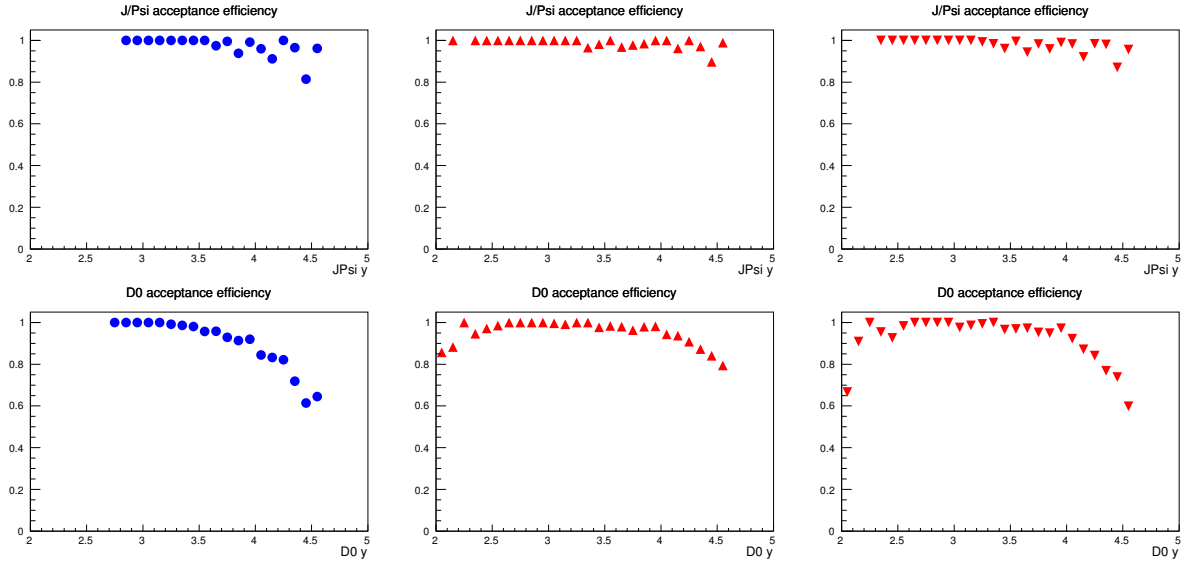
Figure 45: Acceptance cuts efficiencies as a function of rapidity, obtained for $J/\psi \rightarrow \mu^+\mu^-$ (upper plots) and $D^0 \rightarrow K^-\pi^+$ (lower plots) for (from left to right) SMOG2, SMOG_A and SMOG_B.

Table 5: Average estimated acceptance cuts efficiencies for SMOG2 and the two SMOG configurations. The last two columns report the difference between the efficiencies of SMOG2 and SMOG_A ($\Delta\varepsilon_1$) and between those of SMOG2 and SMOG_B ($\Delta\varepsilon_2$), respectively.

Acceptance cuts efficiencies					
	ε_{SMOG2}	ε_{SMOG_A}	ε_{SMOG_B}	$\Delta\varepsilon_1$	$\Delta\varepsilon_2$
$J/\psi \rightarrow \mu^+\mu^-$	91%	96%	93%	**−5%**	**−2%**
$D^0 \rightarrow K^-\pi^+$	78%	92%	83%	**−14%**	**−5%**

9.3 Primary Vertex reconstruction

The PV reconstruction is a crucial step for many analyses and constitutes an important test bench for SMOG2, given the relative distance between the target cell and the VELO. In the MC, the variable $nPVs$ allows to distinguish between reconstructed ($nPVs = 1$) and not-reconstructed ($nPVs = 0$) PVs. The PV reconstruction efficiency is then evaluated as the ratio between the event yields obtained requiring and not-requiring the condition $nPVs = 1$. The ratio is performed considering only truth-matched events within the acceptance. The $nPVs$ variable is shown in Fig. 46 for the two selected physics channels, separately for the three target configurations considered. The average PV reconstruction efficiencies for SMOG2 and SMOG, as well as their differences, are reported in Tab. 6. A drop in the efficiencies below 10 % is obtained for all cases.
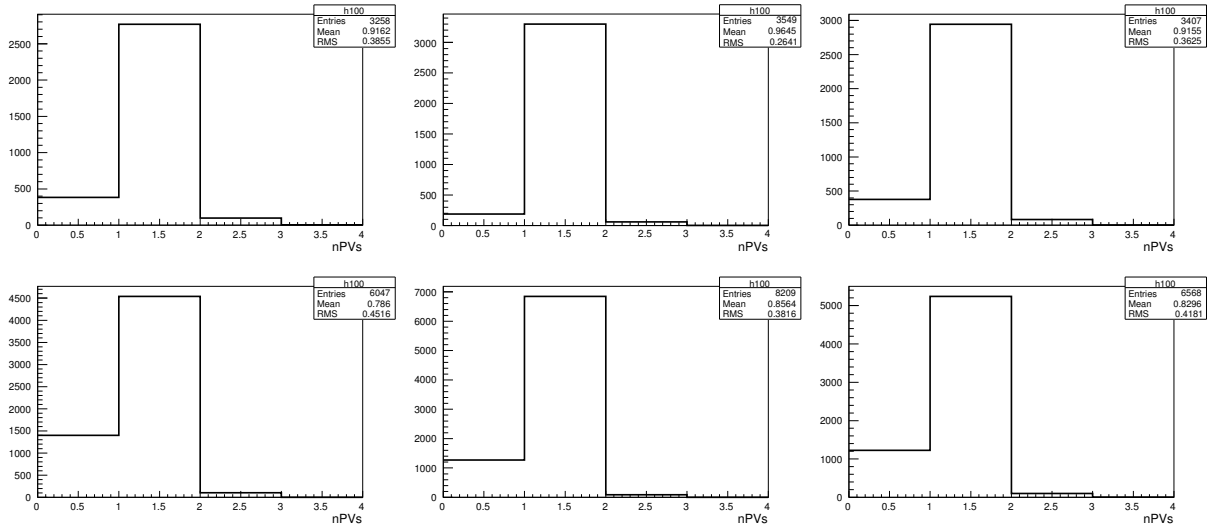
Figure 46: Distribution of the $nPVs$ variable obtained for $J/\psi \rightarrow \mu^+\mu^-$ (upper plots) and $D^0 \rightarrow K^-\pi^+$ (lower plots) for (from left to right) SMOG2, SMOG_A and SMOG_B.

Table 6: Average estimated PV reconstruction efficiencies for SMOG2 and the two SMOG configurations. The last two columns report the difference between the efficiencies of SMOG2 and SMOG_A ($\Delta\varepsilon_1$) and between those of SMOG2 and SMOG_B ($\Delta\varepsilon_2$), respectively.

PV reconstruction efficiencies					
	ε_{SMOG2}	ε_{SMOG_A}	ε_{SMOG_B}	$\Delta\varepsilon_1$	$\Delta\varepsilon_2$
$J/\psi \rightarrow \mu^+\mu^-$	88%	95%	89%	-7%	-1%
$D^0 \rightarrow K^-\pi^+$	77%	84%	81%	-7%	-4%

9.4 PID cuts

The PID cuts efficiencies are obtained as the ratios between the event yields with and without the PID requirements for the decay products. For the two physics channels examined, these are:

- $ProbNNmu > 0.5$ for μ^+ and μ^- ;

- $PIDK > 5$ and $PIDK < 0$ for kaons and pions, respectively.

The ratios are performed considering only truth-matched events within the acceptance and with a reconstructed PV. As expected, there is nearly no difference between the three target configurations within the statistical precision of this study, and $\Delta\varepsilon$ consistent with zero are obtained.

The efficiencies are shown in Fig. 47 as a function of the J/ψ and D^0 rapidity, separately for the three target configurations. The average values are reported in Tab. 7.

9.5 Selection cuts

Several selection cuts are needed in the offline analyses to select the events of interest and to reject as much as possible the background events. Similarly to the PID case described above, the
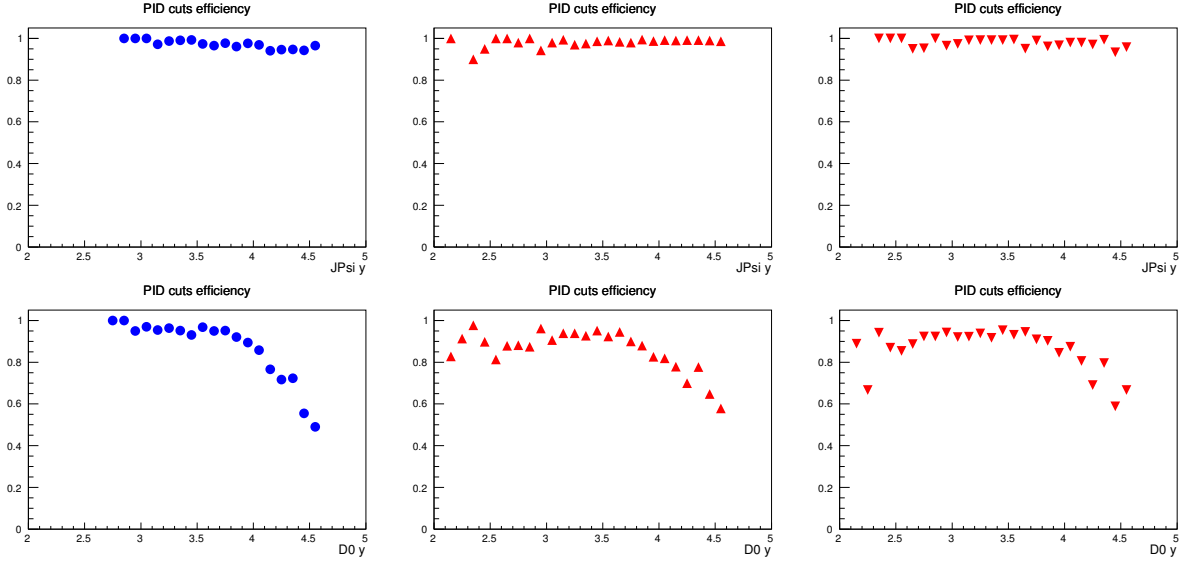
Figure 47: PID cut efficiencies as a function of rapidity, obtained for $J/\psi \rightarrow \mu^+\mu^-$ (upper plots) and $D^0 \rightarrow K^-\pi^+$ (lower plots) for (from left to right) SMOG2, SMOG_A and SMOG_B.

Table 7: Average estimated PID cuts efficiencies for SMOG2 and the two SMOG configurations. The last two columns report the difference between the efficiencies of SMOG2 and SMOG_A ($\Delta\varepsilon_1$) and between those of SMOG2 and SMOG_B ($\Delta\varepsilon_2$), respectively.

PID cuts efficiencies					
	ε_{SMOG2}	ε_{SMOG_A}	ε_{SMOG_B}	$\Delta\varepsilon_1$	$\Delta\varepsilon_2$
$J/\psi \rightarrow \mu^+\mu^-$	96%	98%	98%	**−2%**	**−2%**
$D^0 \rightarrow K^-\pi^+$	86%	86%	86%	**0**	**0**

selection cuts efficiencies are obtained as the ratios between the event yields with and without the selection cuts. For the two physics channels examined the following selection cuts have been used:

- $p_T(\mu^\pm) > 500$ MeV/c,

  $p(\mu^\pm) > 3$ GeV/c,

  $p_T(J/\psi) > 200$ MeV/c,

  2946 MeV $< m_{\mu\mu} < 3246$ MeV,

  $0 < IP(\chi^2) < 6$,

  $0 < DecayVertex(\chi^2) < 16$;

- $p_T(K, \pi) > 250$ MeV/c,

  $p(K, \pi) > 3$ GeV/c,

  $p_T(D^0) > 100$ MeV/c,

46

$$1840 \text{ MeV} < m_{K\pi} < 1900 \text{ MeV},$$
$$0 < IP(\chi^2) < 6,$$
$$0 < DecayVertex(\chi^2) < 16 .$$

The ratios are performed considering only truth-matched events within the acceptance, requiring a reconstructed PV and applying the PID cuts. The selection cuts efficiencies are shown in Fig. 48 as a function of the J/ψ and D^0 rapidity, separately for the three target configurations. The average values are reported in Tab. 8. Also in this case, there is nearly no difference between the three target configurations within the statistical precision of this study.
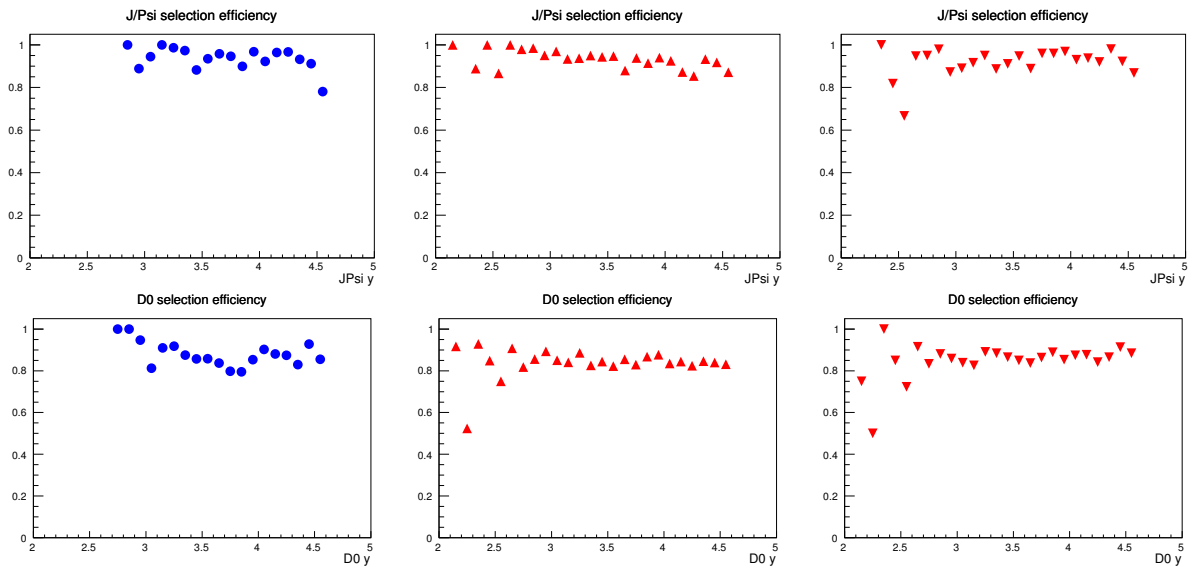

Figure 48: Selection cuts efficiencies as a function of rapidity, obtained for $J/\psi \rightarrow \mu^+\mu^-$ (upper plots) and $D^0 \rightarrow K^-\pi^+$ (lower plots) for (from left to right) SMOG2, SMOG_A and SMOG_B.

Table 8: Average estimated selection cuts efficiencies for SMOG2 and the two SMOG configurations. The last two columns report the difference between the efficiencies of SMOG2 and SMOG_A ($\Delta\varepsilon_1$) and between those of SMOG2 and SMOG_B ($\Delta\varepsilon_2$), respectively.

Selection cuts efficiencies					
	ε_{SMOG2}	ε_{SMOG_A}	ε_{SMOG_B}	$\Delta\varepsilon_1$	$\Delta\varepsilon_2$
$J/\psi \rightarrow \mu^+\mu^-$	93%	92%	93%	+1%	**0**
$D^0 \rightarrow K^-\pi^+$	86%	85%	86%	+1%	**0**

9.6 Trigger cuts

Trigger requirements are applied in order to select the events of interest. For the present study the following trigger requirements were applied for the two physics channels examined, respectively:

- $J/\psi\_L0Muon\_TOS == 1$, $J/\psi\_Hlt1HighMassDimuon\_TOS == 1$;

- $D0\_Hlt1SMOGKPi\_TOS == 1$.

The trigger efficiencies are obtained as the ratios between the event yields with and without the trigger requirements. The ratios are performed considering only truth-matched events within the acceptance, with a reconstructed PV and applying the PID and selection cuts described above. The trigger efficiencies are shown in Fig. 49 as a function of the J/ψ and D^0 rapidity, separately for the three target configurations. The average values are reported in Tab. 9. Also in this case, there is nearly no difference between the target configurations within the statistical precision of this study.
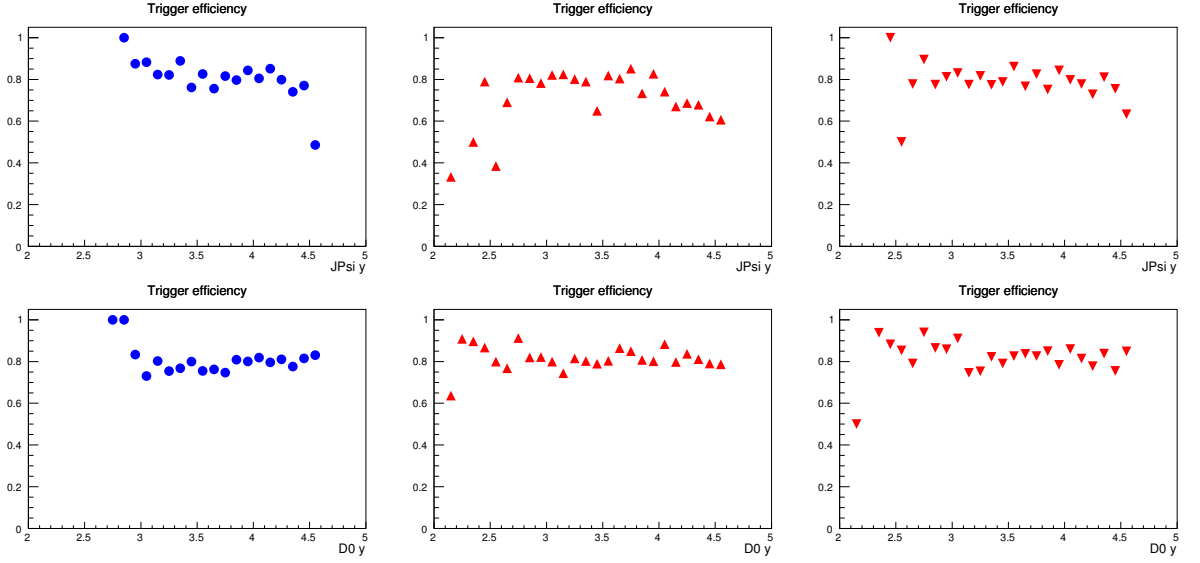

Figure 49: Trigger efficiencies as a function of rapidity, obtained for $J/\psi \rightarrow \mu^+\mu^-$ (upper plots) and $D^0 \rightarrow K^-\pi^+$ (lower plots) for (from left to right) SMOG2, SMOG_A and SMOG_B.

Table 9: Average estimated trigger efficiencies for SMOG2 and the two SMOG configurations. The last two columns report the difference between the efficiencies of SMOG2 and SMOG_A ($\Delta\varepsilon_1$) and between those of SMOG2 and SMOG_B ($\Delta\varepsilon_2$), respectively.

Trigger efficiencies					
	ε_{SMOG2}	ε_{SMOG_A}	ε_{SMOG_B}	$\Delta\varepsilon_1$	$\Delta\varepsilon_2$
$J/\psi \rightarrow \mu^+\mu^-$	79%	76%	79%	**+3%**	**0**
$D^0 \rightarrow K^-\pi^+$	79%	81%	82%	**−2%**	**−3%**

9.7 Global efficiencies

The global efficiencies (for truth-matched events) are obtained for the three target configurations as the ratios between the event yields with and without all requirements discussed above (ac-

ceptance, PV reconstruction, PID and selection cuts, and trigger requirements). Only the track reconstruction requirements are not included here, since based on the MC truth. The global efficiencies are shown in Fig. 50 as a function of the J/ψ and D^0 rapidity, separately for the three target configurations. The average values are reported in Tab. 10.
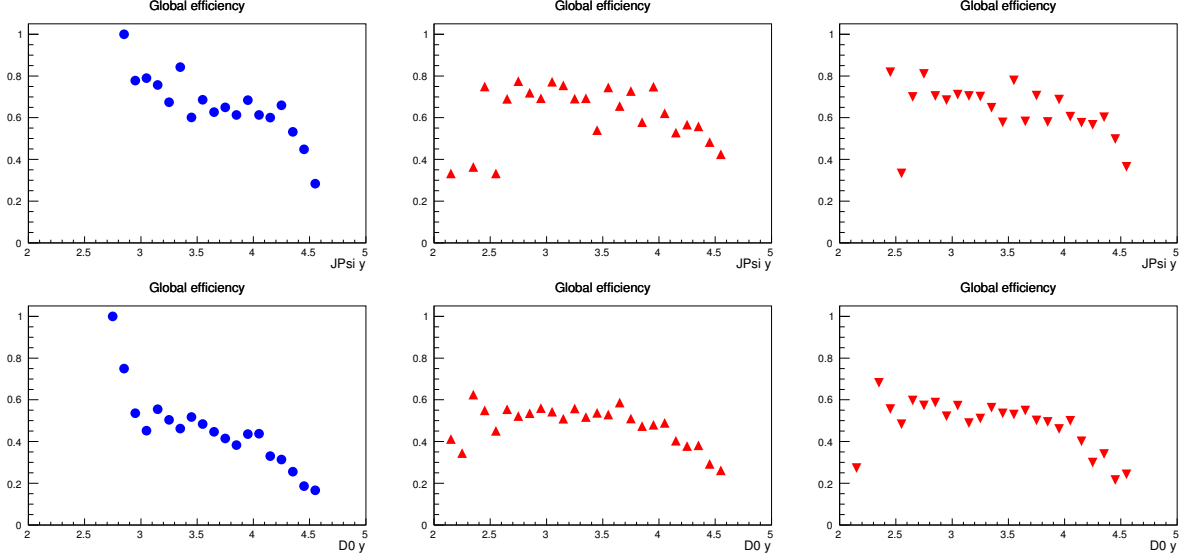

Figure 50: Global efficiencies as a function of rapidity, obtained for $J/\psi \rightarrow \mu^+\mu^-$ (upper plots) and $D^0 \rightarrow K^-\pi^+$ (lower plots) for (from left to right) SMOG2, SMOG_A and SMOG_B.

Table 10: Average estimated global efficiencies for SMOG2 and the two SMOG configurations. The last two columns report the difference between the efficiencies of SMOG2 and SMOG_A ($\Delta\varepsilon_1$) and between those of SMOG2 and SMOG_B ($\Delta\varepsilon_2$), respectively.

Global efficiencies					
	ε_{SMOG2}	ε_{SMOG_A}	ε_{SMOG_B}	$\Delta\varepsilon_1$	$\Delta\varepsilon_2$
$J/\psi \rightarrow \mu^+\mu^-$	58%	63%	60%	**−5%**	**−2%**
$D^0 \rightarrow K^-\pi^+$	35%	46%	41%	**−11%**	**−6%**

10 SMOG2 Projected Performances

Considering the average values in Tab. 10 and assuming same working conditions, one would expect global efficiencies for SMOG2 about 5 % and 10 % smaller than for SMOG, respectively for the two physics channels considered. However, one has to consider that this relatively small drop in efficiency will be largely compensated by the expected increase in luminosity due to the use of a storage cell. The expected areal-density increase factors, calculated analytically under reasonable assumptions, are reported in Tab. 1 for several gas species. An additional important gain factor is represented by the possibility to exploit all the beam bunches for fixed-target collisions, thanks to the well displaced interaction regions for fixed-target and collider modes.

Table 11 reports the signal yields measured with SMOG for several physics channels and the corresponding projected yields for SMOG2, assuming global efficiencies smaller by 10% (with respect to SMOG) and the density scale factors of Tab. 1.

Taking into account the parameters reported in Tab. 1, the luminosity in Run3[15], and the cross sections at 115 GeV and 14 TeV, it is also possible to calculate the collision rate (R) given by SMOG2 with respect to pp. The following selected examples are for H_2 and Ar targets:

$$\frac{R_{H_2}}{R_{pp}} = \frac{\sigma_{pH_2}(115\ GeV) \cdot L_{SMOG2}}{\sigma_{pp}(14\ TeV) \cdot L_{pp}} \simeq 1.3\%, \tag{12}$$

$$\frac{R_{Ar}}{R_{pp}} = \frac{\sigma_{pAr}(115\ GeV) \cdot L_{SMOG2}}{\sigma_{pp}(14\ TeV) \cdot L_{pp}} \simeq 10.6\%. \tag{13}$$

Table 11: SMOG2 projected yields for selected reactions compared to the SMOG ones, measured using a fiducial PVz region of 40 cm, Ref. [5]. The scale factor used for the SMOG2 projections assumes same data-taking periods, same gas flow rate, global efficiency in average 10% smaller, and the areal density scale factors for Ar and He from Tab. 1 corrected by a factor 2 to account for the different fiducial volumes lengths (80 cm vs. 40 cm). The possible significantly larger number of usable bunches is not accounted for.

SMOG2 projected performances							
Reaction	DAQ time	Non coll. bunches	Lumi (nb^{-1})	Decays	SMOG yields	Scale factor	SMOG2 proj. yields
pAr	18 h	684	~ 2	$D^0 \to K^-\pi^+$	6450	62	400 k
				$D^+ \to K^-\pi^+\pi^+$	975		60 k
				$D_s^+ \to K^-K^+\pi^+$	131		8 k
				$D^{*+} \to D^0\pi^+$	2300		140 k
				$\Lambda_c^+ \to pK^-\pi^+$	50		3 k
				$J/\psi^+ \to \mu^+\mu^-$	500		30 k
				$\psi' \to \mu^+\mu^-$	20		1.2 k
pHe	84 h	648	7.6	$J/\psi^+ \to \mu^+\mu^-$	500	19.6	10 k
				$\psi' \to \mu^+\mu^-$	20		0.4 k

11 Planning and responsibilities

In Fig. 51 the Gantt chart of the project with the main steps about the finalization of the R&D, the construction and the installation is reported.

The R&D process has been possible thanks to the involvement of several groups from different institutions. The responsibility of the construction and installation of the target system is in charge of INFN Sezione di Ferrara and INFN Laboratori Nazionali di Frascati. As for SMOG, the operation and maintenance of the GFS remains in charge of the LHC vacuum group.

---

[15]Considering, conservatively, $3 \cdot 10^{14}$ protons per beam.

SMOG2 Time Schedule								
TASKS	**Periods**							
	2019				2020			
	Q1	Q2	Q3	Q4	Q1	Q2	Q3	Q4
1. 2nd cell prototype construction	▮							
2. RF measurements in laboratory		▮						
3. Prototype target stress tests		▮	▮					
4. Pipes and Long cable definition at P8	▮							
5. GFS table construction and test in laboratory				▮	▮	▮		
6. Tests of surface coatings		▮						
7. Final target construction (including 1 spare)			▮	▮				
8. Target installation				▮				
9. GFS installation							▮	
10. Slowcontrol coding			▮	▮	▮	▮	▮	
11. Trigger coding				▮	▮	▮	▮	▮

Figure 51: Gantt chart of the SMOG2 project with the main steps of R&D, construction and installation.

12 Conclusions

SMOG2 will result in a significant improvement of the performances of the LHCb fixed-target system with respect to the present SMOG system, opening to innovative and fundamental measurements in regions of the kinematic plane mainly unexplored. The R&D performed shows the full compatibility with the LHCb detector, requiring basically no change. Besides, the studies performed about vacuum, impedance, aperture and other machine issues did not identify any show-stopper from the LHC side.

The R&D will continue with measurements and laboratory tests using prototypes and refined simulations in strong collaboration with the other LHC and LHCb groups involved in the machine and spectrometer upgrade.

13 Acknowledgments

References

[1] C. Barschel, *Precision luminosity measurements at LHCb with beam-gas imaging*, CERN-THESIS-2013-301, RWTH Aachen University, 2014.

[2] R. Aaij *et al.* [LHCb Collaboration], *Performance of the LHCb Vertex Locator*, JINST **9** (2014) P09007, arXiv:1405.7808;

[3] R. Aaij *et al.* [LHCb Collaboration], *Precision luminosity measurements at LHCb*, JINST **9** (2014) P12005, arXiv:1410.0149 [hep-ex].

[4] M. Ferro-Luzzi, *Proposal for an absolute luminosity determination in colliding beam experiments using vertex detection of beam-gas interactions*, Nucl. Instrum. Meth. **A553** (2005) 388.

[5] R. Aaij *et al.* [LHCb Collaboration], *First measurements of charm production in fixed-target configuration at the LHC*, arXiv:1810.07907 [hep-ex] (submitted to PRL).

[6] R. Aaij *et al.* [LHCb Collaboration], *Measurement of antiproton production in pHe collisions at $\sqrt{s_{NN}} = 110$ GeV*, Phys. Rev. Lett. 121 (2018), 222001, arXiv:1808.06127 [hep-ex].

[7] PBC Report, *Physics opportunities with the fixed target program of the LHCb experiment using an unpolarized gas target*, LHCb-PUB-2018-015.

[8] P. Collins *et al.*, *The LHCb VELO upgrade*, Nucl. Instrum. Meth. **A636** (2011), s185.

[9] [LHCb Collaboration], *LHCb VELO Upgrade Technical Design Report*, CERN-LHCC-2013-021; LHCB-TDR-013.

[10] R.B. Appleby et al., *VELO aperture considerations for the LHCb Upgrade*, LHCb-PUB-2012-018, https://cds.cern.ch/record/1498738?ln=fr

[11] E. Steffens and W. Haeberli, *Reports on Progress in Physics Polarized gas targets*, Rep. Prog. Phys. **66** (2003) 1887.

[12] C. Boscolo Meneguolo et al., *Calculation of the allowed aperture for a gas storage cell in IP8*, CERN-PBC-Notes-2018-008.

[13] Velo group meeting (indico 698038), presentation:
https://indico.cern.ch/event/698038/contributions/3124154/attachments/1708520/2753539/
VELO_Wire_Measurements_310818_Rev2_CV.pdf .

[14] IWG meeting #24 (indico 764129), presentation:
https://indico.cern.ch/event/764129/contributions/3171803/attachments/1732004/2799709/
VELO_Wire_Measurements_IWG.pdf .

[15] IWG meeting #25 (indico 765714), presentation:
https://indico.cern.ch/event/765714/contributions/3178576/attachments/1736758/2809374/
Complete_VELO_with_SMOG_181018.pdf .

[16] IWG meeting #25 (indico 765714), presentation: https://indico.cern.ch/event/765714/contributions/3178582/attachments/1736779/2809412/LHC_SMOG2.pdf .

[17] B.K. Popovic, *VELO with SMOG2 Impedance-based Heating Localization Analysis*, CERN-PBC-Notes-2019-003; PBC-IFT meeting (indico 797685) presentation: https://indico.cern.ch/event/797685/contributions/3314381/attachments/1798905/2933516/PBC-FT_Meeting_VELO_Heating_FINAL.pdf .

[18] HERMES Collaboration, *HERMES TDR*, DESY PRC 93/06, and Ref. therein: Ref. [2.3.10] Piwinski 1992, and Ref.[2.3.11], Bane et al, AIP Conf. Proc. **127** (1985) 875.

[19] K. Poland, L. Mether, PBC-IFT meeting (indico 797685) presentation: https://indico.cern.ch/event/797685/contributions/3320602/attachments/1798878/2933458/PBC-FT_20190220_ecloud.pdf, PBC note in preparation.

[20] A. Airapetian et al., HERMES Collaboration, NIMA **540** (2005) 68–101.

[21] G. Ciullo et al., Journal of Physics: Conference Series **295** (2011) art. n. 012150.

[22] A. Gade, *Unpolarized Gas Feeding System – HERMES Operational Manual*, HERMES Internal Note – June 2004 http://www.fe.infn.it/u/ciullo/UGFS/UGFS_manual_2006_updated.pdf .

[23] G. Corti, M. Lieng, R. Jacobsson, *Requirement for Machine Induced Backgrounds Studies in LHCb*, LHCb-INT-2009-017.

[24] G. Corti et al., *Simulation of Machine Induced Background in the LHCb experiment: Methodology and implementation*, IEEE Nuclear Science Symposium & Medical Imaging Conference (2010) 701.

[25] M.H. Lieng, *LbMIB: A Machine Induced Background Generator Tool for Gauss*, LHCb-INT-2011-015.

[26] J. Allison *et al.* (GEANT4 Collaboration), *GEANT4 developments and applications*, IEEE Trans. Nucl. Sci. **53**, N.1 (2006) 270.

[27] S. Agostinelli *et al.* (GEANT4 Collaboration), *GEANT4: A simulation toolkit*, Nucl. Instrum. Meth. A **506** (2003) 250.

[28] J. Allison *et al.* (GEANT4 Collaboration), *Recent developments in Geant4*, Nucl. Instrum. Meth. A **835** (2016) 186.

[29] T. Sjostrand, S. Mrenna, and P.Z. Skands, *A brief introduction to PYTHIA 8.1*, Comput. Phys. Commun. **178** (2007) 852, arXiv:0710.3820.

[30] T. Sjostrand, S. Mrenna, and P.Z. Skands, *PYTHIA 6.4 physics and manual*, JHEP **05**, 026, arXiv:hep-ph/0603175.

[31] T. Pierog *et al.*, *EPOS LHC: Test of collective hadronization with data measured at the CERN Large Hadron Collider*, Phys. Rev. C **92** (2015) 034906.

[32] D. J. Lange, *The EvtGen particle decay simulation package*, Nucl. Instrum. Meth. **A462** (2001) 152.

[33] M. Clemencic *et al.*, *The LHCb simulation application, Gauss: Design, evolution and experience*, J. Phys. Conf. Ser. **331** (2011) 032023.

[34] The LHCb collaboration. The boole project. http://lhcb-release-area.web.cern.ch/LHCb-release-area/DOC/boole/

[35] The LHCb collaboration. The moore project. http://lhcb-release-area.web.cern.ch/LHCb-release-area/DOC/moore/

[36] The LHCb collaboration. The brunel project. http://lhcb-release-area.web.cern.ch/LHCb-release-area/DOC/brunel/

[37] The LHCb collaboration. The davinci project. http://lhcb-release-area.web.cern.ch/LHCb-release-area/DOC/davinci/